Journal of Catalysis 271 (2010) 325–342

Contents lists available at ScienceDirect

Journal of Catalysis

journal homepage: www.elsevier.com/locate/jcat

Ethanol synthesis from syngas over Rh-based/SiO_2 catalysts: A combined experimental and theoretical modeling study

Donghai Mei [a,*], Roger Rousseau [a], Shawn M. Kathmann [a], Vassiliki-Alexandra Glezakou [a], Mark H. Engelhard [b], Weilin Jiang [a], Chongmin Wang [b], Mark A. Gerber [c], James F. White [c], Don J. Stevens [c]

[a] Chemical and Materials Sciences Division, Pacific Northwest National Laboratory, Richland, WA 99352, USA
[b] Environmental Molecular Science Laboratory, Pacific Northwest National Laboratory, Richland, WA 99352, USA
[c] Chemical and Biological Process Division, Pacific Northwest National Laboratory, Richland, WA 99352, USA

ARTICLE INFO

Article history:
Received 28 September 2009
Revised 4 February 2010
Accepted 13 February 2010
Available online 19 March 2010

Keywords:
Syngas
Ethanol
Rhodium nanoparticles
Manganese
Promoters
Density functional theory
Kinetic Monte Carlo

ABSTRACT

Catalytic conversion of biomass-derived synthesis gas to ethanol and other C_2^+ oxygenates has received considerable attention recently due to the strong demands for alternative, renewable energy sources. Combining experimental measurements with first-principles-based kinetic modeling, we investigated the reaction kinetics of ethanol synthesis from CO hydrogenation over SiO_2 -supported Rh/Mn alloy catalysts. We find that an Mn promoter can exist in a binary alloy with Rh and play a critical role in lowering the CO insertion reaction ($CO + CH_x$ ($x = 1–3$)) barriers thus improving the selectivity toward ethanol and other C_2^+ oxygenates, although the barrier toward methane formation is unaffected. The postulation of supported Rh/Mn alloy nanoparticle being the active phase is supported by our experimental characterization using X-ray photoelectron spectroscopy, transmission electron microscopy, and X-ray diffraction of practically used Rh/Mn/SiO_2 catalysts. First-principles density functional theory (DFT) calculations further confirmed that the binary Rh/Mn alloy is thermodynamically more stable than the mixed metal/metal oxides under the reducing reaction condition. The reaction kinetics of CO hydrogenation to ethanol on the three-dimensional Rh/Mn nanoparticle under experimental operating conditions was studied using kinetic Monte Carlo (KMC) simulations. The simulated reaction kinetics is qualitatively consistent with experimental observations. Finally, the effects of various promoters (M = Ir, Ga, V, Ti, Sc, Ca, and Li) on the CO insertion reaction over Rh/M alloy nanoparticles were investigated using DFT calculations. We found alloying the promoters with the electronegativity difference, $\Delta\chi$, between the promoter (M) and Rh being 0.7 is the most effective in lowering the barriers of CO insertion reaction, which leads to higher selectivity to ethanol. This conclusion is in excellent accord with the reported catalytic performance of CO hydrogenation over Rh-based catalysts with different promoters. We believe that the electronegativity difference criterion is very useful in improving the catalytic performance using transition metal-based catalysts for ethanol synthesis from CO hydrogenation.

1. Introduction

The production of renewable fuels such as ethanol has received considerable attention in recent years for its use in automobiles and as a potential source of hydrogen for fuel cells [1–3]. Currently, ethanol is produced primarily by fermentation of biomass-derived sugars [4]. Gasification of biomass to syngas (CO, CO_2, H_2, H_2O), followed by catalytic conversion, provides a promising alternate route to produce ethanol in large quantities [5]. In spite of the substantial amount of research on this catalytic conversion route, no commercial process exists due to the challenging chemical and technological barriers [6]. Low yield and poor selectivity for ethanol production from syngas remain the major hurdles associated with the use of known catalysts [6]. In order to make this catalytic conversion route commercially attractive, it is essential to develop more effective catalysts.

Among the existing catalyst candidates, supported Rh-based catalysts are known to preferentially convert syngas to C_2^+ oxygenates relative to C_1 oxygenates [7–10]. This is due to the fact that supported Rh catalyst particles could simultaneously adsorb CO in both molecular and dissociated states [9,10]. Hydrogenation of CO over SiO_2-supported Rh catalysts yield a wide variety of products including methane and higher hydrocarbons, methanol, ethanol and higher alcohols, acetaldehyde, acetic acid, and other higher oxygenates, depending upon the reaction conditions, supports and promoters [7–10]. A substantial amount of experimental work has been performed to investigate the promoting effects of adding the

* Corresponding author.
E-mail address: donghai.mei@pnl.gov (D. Mei).

0021-9517/$ - see front matter © 2010 Elsevier Inc. All rights reserved.
doi:10.1016/j.jcat.2010.02.020

second metals such as Mn on the supported Rh catalysts, in order to improve activity and selectivity [5,6,11,12]. For example, Ellgen et al. studied CO hydrogenation over Rh/SiO_2 and $Rh/Mn/SiO_2$ at high pressures (30–200 atm) and temperatures between 250 and 300 °C in a back-mixed reactor with unity H_2/CO ratio [13]. Over 90% of CO was converted to methane, acetic acid, acetaldehyde, and ethanol after reaction. They found that the addition of relatively small quantities of Mn into Rh/SiO_2 increase the total activity by an order of magnitude. Both formation rates of methanol and C_2^+ oxygenates including acetic acid, acetaldehyde, and ethanol increased while the selectivity seemed to be insensitive to the Mn promoter. The same apparent activation energy of 24 kcal/mol was reported for $Rh/Mn/SiO_2$ catalysts with two different Rh/Mn ratios. The reaction orders of CO and H_2 were about −0.48 to −0.33 and +0.58 to +0.64, respectively [13]. Although it is well known that the addition of Mn into Rh/SiO_2 catalysts promotes the activity of CO hydrogenation, the role and the state of Mn in the $Rh/Mn/SiO_2$ catalyst are still unclear. Using electron spin resonance (ESR) spectroscopy, Wilson et al. suggested that Mn might exist as Mn^{2+} with Rh^+ on the silica support [14]. A similar conclusion was obtained by van den Berg et al. [15]. They found that manganese oxides that partially cover the Rh particle surface cannot be completely reduced by pretreatment with hydrogen at 500 °C. Conversely, Luo et al. studied the role of Mn as a promoter in Rh-based catalysts and found that Rh can promote the reduction of Mn. They claimed that the presence of Mn promoter increases hydrogen spillover, which can then take part in the activation of adsorbed CO [16]. Thus, the clarification of the chemical state of the Mn promoter and elucidation of its role are critical for understanding how the promoter affects the catalytic performance in ethanol synthesis from syngas over the supported Rh/Mn catalysts.

The reaction mechanism for CO hydrogenation to ethanol over the Rh-based catalysts is very complicated [17–19]. It generally involves CO dissociation, hydrogenation of C_1 species into CH_x, CO insertion into adsorbed CH_x to form acyl species (CH_xCO) and their subsequent hydrogenation. Bowker proposed an acetate reaction route for ethanol formation from CO hydrogenation [17]. The acetate formed by acyl oxidation was suggested as the key reaction intermediate in the reaction network (see Fig. 1). Alternatively, ethanol also can be formed via acetaldehyde that is generated by CH_3 insertion into CO, followed by further hydrogenation [17–19]. Another reaction route for CO hydrogenation to ethanol was based on the insertion of CH_2 into adsorbed CH_2–O species forming ethylene oxide (CH_2–CH_2–O) intermediates and then further hydrogenation into ethanol [20]. Very recently, Choi and Liu investigated ethanol synthesis mechanism from CO hydrogenation on Rh(1 1 1) using density functional theory (DFT) calculations [21]. In their proposed mechanism, CO hydrogenation to formyl (HCO) instead of CO dissociation is the rate-limiting step due to the extremely high barrier of 3.72 eV for CO dissociation on Rh(1 1 1). HCO further hydrogenates to methoxy (CH_3O) and then dissociates into CH_3 + O. The key reaction intermediate leading to ethanol formation is acetyl (CH_3CO) that is formed by CH_3 insertion into CO [21]. As such, the selectivity of ethanol on Rh(1 1 1) largely depends on the reaction barriers of CH_3 + CO and CH_3 + H. Rh(1 1 1) is then suggested as the active surface for ethanol synthesis from CO hydrogenation. CO insertion could occur on Rh^0 sites over the Rh(1 1 1) surface. It has to be mentioned that the above theoretical calculations by Choi and Liu [21] do not rule out that Rh^+ sites might be the more active sites for CO insertion. According to our experimental observation, the smaller supported Rh particles interacting with the SiO_2 support might contain Rh^+ sites, which seems to more active for C_2^+ oxygenates formation. This is consistent with previous experiments by Somorjai [22] and Chuang et al. [23,24].

In this work, we combine different reaction routes reported in previous studies with hundreds of elementary steps as the reaction network shown in Fig. 1. We focus on the catalytic conversion of syngas to C_2^+ oxygenates with special emphasis on ethanol. We believe that the reactivities of the last methanation step (CH_3 + H) that lead to the major by-product methane and the CO insertion into CH_x steps that lead to the desired C_2^+ oxygenates over Rh-based catalysts are the crucial steps in the entire reaction network of CO hydrogenation to ethanol. To the best of our knowledge, there are no theoretical studies focusing on how these crucial steps are affected by various promoters. The fundamental insight into theoretical investigation is essential not only for understanding how the catalyst functions, but also serves as a basis for the selective modification of the catalyst to improve catalytic performance towards the desired products.

Synthesis gas can be catalytically converted to ethanol as well as other value-added fuels. Experimental efforts aiming at improving catalyst space–time yield (STY) and selectivity can benefit from the molecular-level insights obtained from quantum computational chemistry and kinetic modeling. In conjunction with our experimental measurements of CO hydrogenation to ethanol and C_2^+ oxygenates over the $Rh/Mn/SiO_2$ catalysts, we studied the activation barriers and reaction energies of CO insertion reactions and methane formation on the pure Rh and the Mn-doped Rh alloy nanoparticles using first-principles DFT method. The model Rh and bimetallic Rh/Mn catalyst nanoparticles used in this work were guided by the atomistic and structural information generated from the experimental characterization such as X-ray photoelectron spectroscopy (XPS), X-ray diffraction (XRD), and transmission electron microscopy (TEM). We also calculated the binding energies of some of key reaction intermediates on Rh and Rh/Mn nanoparticles using DFT. These intrinsic kinetic parameters were subsequently incorporated with the unity bond index quadratic exponential potential (UBI-QEP) method [25] to be fed into a kinetic Monte Carlo (KMC) simulation model to investigate the reaction kinetics of CO hydrogenation to ethanol over the three-dimensional Rh/Mn nanoparticle catalysts. The KMC-simulated reaction kinetics are then compared directly to our experimental results, as well as those from the literatures. Except for Mn, the effects of other promoters on the catalytic activity and selectivity of ethanol formation over SiO_2 supported Rh catalysts were also investigated [6,12,26–29]. The enhanced activity was found using Ti and V promoters, while Li would improve the selectivity toward C_2^+ oxygenates [6]. Very recently, the effects of different promoters for CO hydrogenation on Rh/SiO_2 were investigated by Goodwin et al. [26,28,29]. They found that the primary promoting effect of La, V, and Fe are different. For example, the addition of La will enhance CO adsorption and CO insertion while adding V into Rh increases the CO dissociation and hydrocarbon chain growth [29]. As such, we studied the effects of different promoters such as Ir, Ga, V, Ti, Sc, Ca, and Li on the CO insertion into CH reaction. We suggest that the electronegativity difference between Rh and the promoter plays an important role in enhancement of ethanol selectivity by facilitating the CO insertion reaction. We conclude by discussing the ramifications of our findings upon possible directions for improving the catalyst performance in these systems.

2. Experimental section

2.1. Catalyst preparation

The $Rh/Mn/SiO_2$ catalyst, consisting of 5.56% Rh and 1.69% Mn by weight, was prepared using the incipient wetness technique with rhodium and manganese nitrate precursors. Davisil 645 high surface-area SiO_2 (−60/+100 mesh) was pretreated by calcination at 500 °C for 2 h with ramping up at 5 °C/min during heating and ramping down at 10 °C/min during cooling. The appropriate quan-

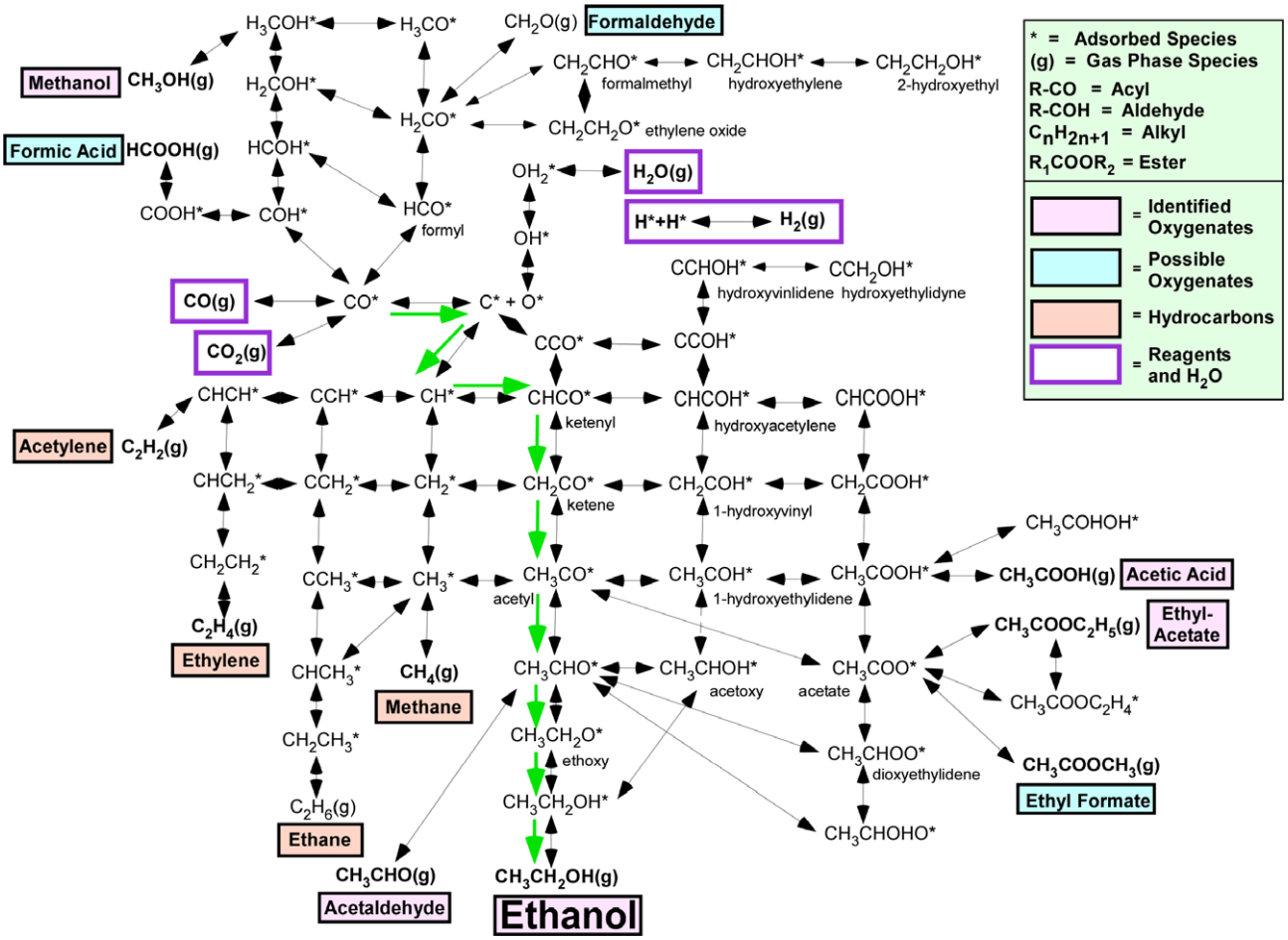

Fig. 1. Reaction mechanism network of CO hydrogenation forming ethanol. The optimal reaction pathway is marked in green. (For interpretation of the references to color in this figure legend, the reader is referred to the web version of this article.)

tities of a rhodium nitrate solution (10 wt.% Rh concentration in solution) and manganese nitrate tetrahydrate were combined with enough deionized water to bring the total volume of the impregnation solution to the water adsorption pore volume of the support. The solution was impregnated with the silica in drop-wise fashion and then dried overnight at 110 °C. The dried catalyst was calcined at 400 °C. The catalyst was reduced using a 10% H_2 in N_2 gas mixture, heating the catalyst to 220 °C at 2.5 °C/min, holding at that temperature for 1 h, then heating the catalyst from 220 °C to 260 °C at 1 °C/min and held at 260 °C overnight.

2.2. Characterization of catalysts

2.2.1. X-ray photoelectron spectroscopy (XPS)

XPS measurements were performed using a Physical Electronics Quantum 2000 Scanning ESCA Microprobe. This system uses a focused monochromatic Al Kα X-rays (1486.7 eV) source and a spherical section analyzer. The instrument has a 16-element multichannel detector. The X-ray beam used was a 100 W, 100 μm diameter beam that was rastered over a 1.3 mm by 0.2 mm rectangle on the sample. The X-ray beam is incident normal to the sample and the photoelectron detector was at 45° off-normal using an analyzer angular acceptance width of 20° × 20°. High-energy resolution spectra were collected using pass energy of 46.95 eV. For the Ag_3 $d_{5/2}$ line, these conditions produced full width at half maxima (FWHM) of better than 0.98 eV. The binding energy (BE) scale is calibrated using the Cu_2 $p_{3/2}$ feature at 932.62 ± 0.05 eV and Au 4f at 83.96 ± 0.05 eV for known standards. The sample experienced variable degrees of charging. Low-energy electrons at ~1 eV, 20 μA, and low energy Ar^+ ions were used to minimize this charging.

2.2.2. Transmission electron microscopy (TEM)

The sample was prepared by dusting the powder particles on 200-mesh TEM grids minimizing any artificial change to the samples. High-resolution TEM analysis was carried out on a Jeol JEM 2010 microscope fitted with a LaB_6 filament and an acceleration voltage of 200 kV. The point-to-point resolution of the microscope is 0.194 nm. Elemental composition of the sample was analyzed using energy dispersive X-ray spectroscopy (EDS) that attached to the microscope (Oxford, ISIS analysis system). All the images were recorded using a 1 k by 1 k CCD camera and processed using Digital Micrograph (Gatan, USA).

2.2.3. X-ray diffraction (XRD)

XRD measurements were performed for fresh and used powders of sample S3 at room temperature using the Philips X'Pert multipurpose diffractometer (MPD), operating at 45 kV and 40 mA with a fixed Cu anode. Symmetric scans with 2θ = 10–80° at a step size of 0.05° were applied. The duration for each step was 35 and 6 s for the fresh and used, respectively. Data analysis was carried out based on software JADE (version 8.5) from Materials Data Inc. and PDF4+ database from ICSD. For more details on the XPS, TEM, and XRD characterization equipment in the Environmental

Molecular Sciences Laboratory (EMSL) at PNNL please see http://www.emsl.pnl.gov/capabilities/instrumentList.jsp.

2.3. Density functional theory (DFT) calculations

DFT calculations were carried out with a gradient corrected functional for exchange and correlation [30] as implemented in the CP2K code [31–33] (freely available at http://cp2k.berlios.de). Core electrons are modeled as norm-conserving pseudopotentials, and the wavefunctions expanded in a double-Zeta Gaussian basis set with a plane wave auxiliary basis of 300 Ry cutoff energy. Reactions are modeled on a (1 1 1)-like surface facet on a 10 Å in diameter Rh-based nanoparticle, which is placed in an 18 Å cubic box with periodic boundary conditions with a minimal distance of 8 Å between the catalytic nanoparticle (and adsorbate) and its nearest neighboring image. Calculation of all reaction coordinates was performed using the climbing image nudged elastic band method (CI-NEB) employing 7 system replicas [34,35].

2.4. Catalyst performance measurements

CO hydrogenation over the $Rh/Mn/SiO_2$ catalyst in the temperature range (255–305 °C) was measured using a bench-scale tubular reactor with the operating pressures up to 1200 psig and temperatures up to 450 °C. The catalyst chamber was 1.67 cm long (in selected tests the space was 0.215 cm long) and 1/4 inch in diameter. A 1/16 inch (0.159 cm) outer diameter thermocouple sheath extended through the center of the reactor, creating an annulus-shaped catalyst chamber. Two thermocouples inside the sheath were spaced so that one was at the center of the catalyst bed and the other just upstream of the catalyst bed. For a typical experiment, the $Rh/Mn/SiO_2$ catalyst was loaded into the reactor and its net weight determined. The reactor was placed in the reactor system and reduced in place at atmospheric pressure. The reactor was cooled after catalyst reduction, and the desired reaction syngas feed rate and pressure were established. The reactor was heated up slowly to a temperature at which the reaction rate was significant and kept there for at least 24 h to allow the catalyst to age. The product stream was directed through the bypass cold trap during this time. After aging the catalyst, the product stream was redirected through the sample cold trap for a period sufficient for at least 10 bed volumes of gas feed (based on the operating pressure and gas feed rate) to pass through the cold trap. This period of time provides a representative gas sample and a sufficiently large liquid sample for subsequent analysis. The operating conditions were recorded before sampling with two or more grab samples of product gas obtained and analyzed in a gas chromatograph (GC) along with a feed gas sample and a calibration gas sample. The liquid recovered from the cold trap was weighed and, if two phases were present, separated into an aqueous phase and an organic phase. The weighed organic phase was not analyzed and was assumed to have a composition comparable to hexane for purposes of a carbon balance. The weighed aqueous phase was analyzed using high pressure liquid chromatography (HPLC) to quantify the C_1 to C_4 oxygenates (principally alcohols, acids, aldehydes, esters, and any other significant peaks identified by the HPLC). After sampling, a new set of conditions (temperature and feed rate) was established and another cold trap sample collected at the new conditions. This procedure was repeated until a representative set of conditions was obtained to evaluate catalyst performance in terms of the STY, single-pass carbon selectivity, and conversion. The gas mixture consisted of H_2, CO, trace amount of CO_2, and N_2 (4% for each component). The H_2/CO ratio in the experiments was kept at 1.9. The gross hourly space velocity (GHSV) varies from 7500 to 15,000 $L/L_{cat}/h$ in our experiments for studying the effect of GHSV on the catalytic performances such as space–time yields (STYs) and carbon selectivity.

3. Experimental results and discussion

3.1. Catalyst characterization

To gain some insight into the structure of the catalyst, we performed careful characterization of several samples of fresh catalyst (prior to reduction) and used catalyst after reaction. It is noted that these measurements were performed *ex situ* (after exposure to air where oxidation may occur), and it is expected that only qualitative statements about the nature of the catalyst under reducing *in situ* conditions may be inferred by extrapolating the changes in the catalyst particles before and after their use.

XPS measurements were performed on both fresh and used catalyst samples. The typical results are presented in Fig. 2. The compo-

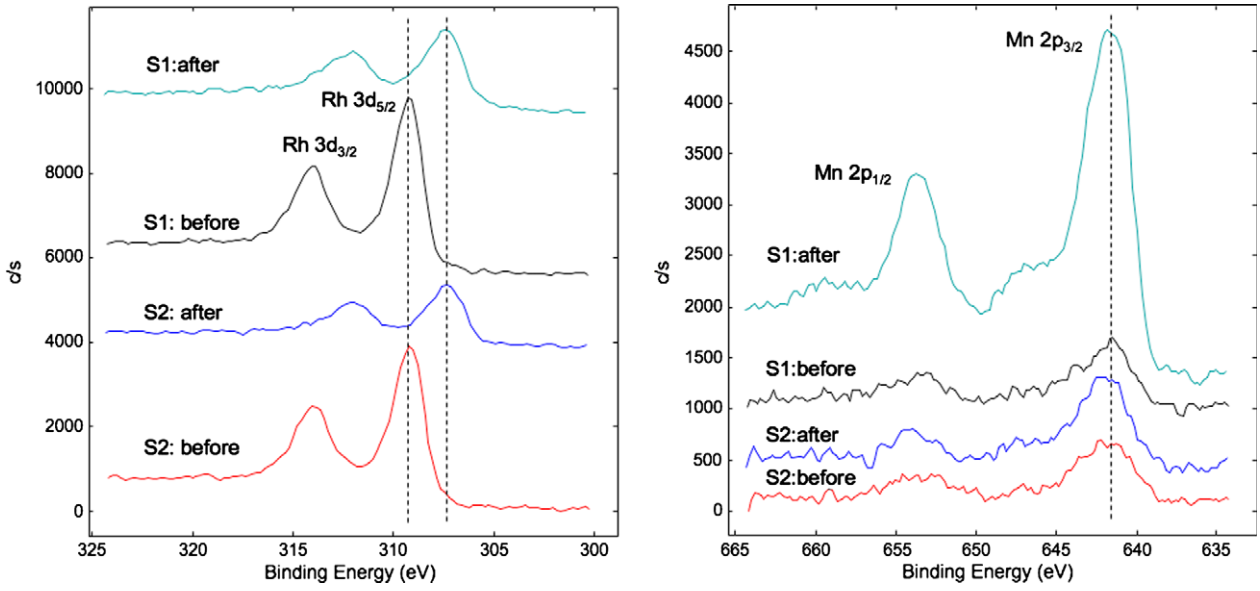

Fig. 2. XPS results of the $Rh/Mn/SiO_2$ catalyst samples 1 and 2 (S1 and S2).

sitions of both catalyst samples used in the incipient wetness technique for both samples are 5.56% Rh and 1.69% Mn by weight. In general for all the samples studied, the XPS analysis shows that Rh exists as Rh_2O_3 (typical XPS Rh $3d_{5/2}$ at 309.2 eV) in the fresh catalyst sample but it is reduced to metallic Rh (Rh^0 at 307.4 eV). This observation is consistent with the interpretation that Rh exists as metal particles under reducing *in situ* conditions. The situation for Mn is less resolved due to the similarity between the *2p* core hole energy between MnO and metallic Mn^0. Although it is highly likely that Mn exists as the Mn^{2+} oxide (Mn $2p_{3/2}$ at 641 eV) for the fresh material, it is not clear if it has been partially reduced in the used sample. The XPS spectra around the $2p_{3/2}$ peak between 645 eV and 638 eV cannot be deconvoluted into various Mn components of the signal (from NIST: Mn = 638.8 to 641.0 eV, MnO = 640.3 to 642.5 eV, MnO_2 = 641.1 to 643.4 eV, Mn_2O_3 = 641.2 to 642.8 eV, Mn_3O_4 = 641.1 to 641.9 eV) with the current spectra. This suggests that a small fraction of Mn may have been reduced during the reducing environment in the catalyst preparation or in the operating conditions and may exist in the metallic state within the metallic Rh particle. Also we must acknowledge that Mn oxides may exist in addition to the metallic Rh and RhMn phases. TEM results of a representative fresh and used $Rh/Mn/SiO_2$ catalyst sample (Sample 3, S3) that were shown in Fig. 3 suggested that an alloyed Rh/Mn particle is formed during the catalyst production/operation where the Rh (and possibly Mn) is reduced. This is in good accord with the observations from XPS. The typical Rh-rich particles are well dispersed on the silica with approximate diameter of 2 nm. For the used catalyst samples, only the larger Rh metal particles were found. No pure Mn metal particles were found after reaction though MnO particles are observed in both fresh and used catalysts.

Fig. 4 shows the representative diffraction patterns of the fresh and used samples, which appear to be very different. The top XRD panel shows the diffraction pattern for the fresh S3, primarily arising from Rh_2O_3, Mn_2O_3, and SiO_2 which matches well with our observations from XPS and TEM. Crystalline phases of pure metals or metal alloys are not observed within the detection limit. Since the diffraction peaks are very broad, the sizes of the crystallites are extremely small (<1 nm), making the powder appears to be an amorphous material. The overall diffraction pattern is further complicated with peak overlapping. Some of the possible minor phases of those materials are submerged in the pattern and this cannot be identified. The bottom XRD panel showed the diffraction pattern for the used S3 sample with well-resolved peaks. Data analysis indicated that in addition to SiO_2 that remained unchanged after use, the primary phase of the used powder is pure Rh possibly with Mn_3Rh inclusions. The Mn diffraction pattern from the database was also marked in Fig. 4 (bottom panel) with its perfect (1 1 1) peak clearly off from those of Rh or Mn_3Rh. Since the (1 1 1) reflection can be well fitted with a single peak, the amount of the Mn phase, if any, is not expected to be significant in the used sample. The metal oxides (Rh_2O_3 and Mn_2O_3) that are

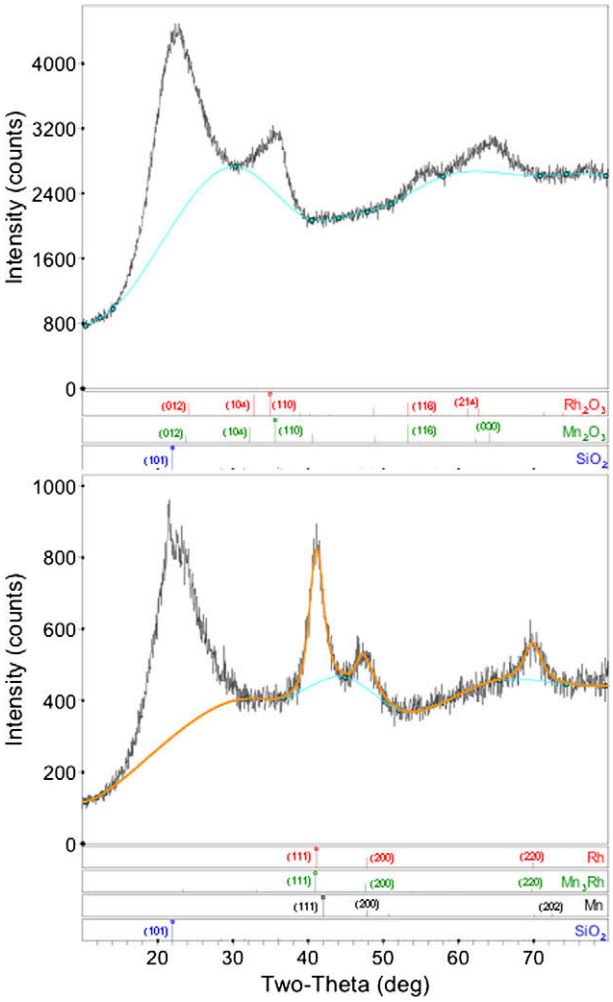

Fig. 4. XRD measurements of S3. The top panel shows S3: before with patterns arising from Rh_2O_2, Mn_2O_2, and SiO_2. The bottom panel shows S3: after with patterns arising from pure Rh, possible Mn_2Rh, and SiO_2.

the components of the fresh S3 sample were not also observed in the used S3 sample. The averaged size of the Rh crystallites in the used S3 sample is estimated to be about 3 nm based on the full-width-at-half-maximum (FWHM) of the (1 1 1) reflection peak using Scherrer formula. The XRD data in Fig. 4 thus suggests that the mixed metal oxides are reduced to pure Rh metal with possible Rh/Mn alloys during the catalyst aging processes. The formed metallic phase further evolves into larger crystallites via aggregation on the support.

In summary, XRD, TEM, and XPS measurements clearly show that the Rh oxide phase of the catalyst is reduced to form Rh metal

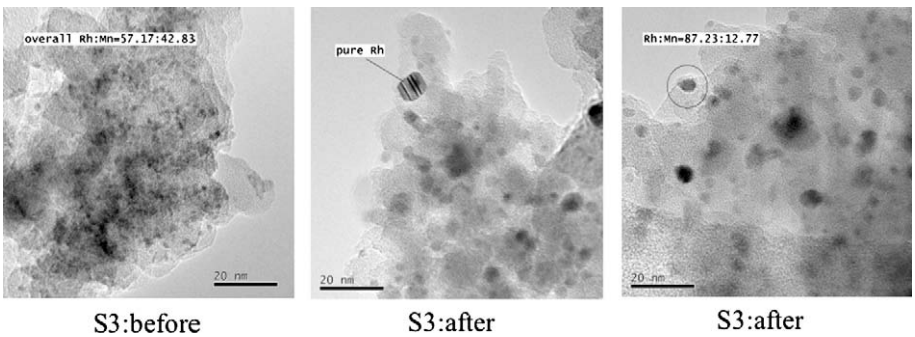

Fig. 3. TEM images of the $Rh/Mn/SiO_2$ catalyst sample 3 (S3).

nanoparticles during the reduction and/or operation. The oxidation state of Mn in the Rh/Mn/SiO_2 catalysts is still not clear although some of previous experiments suggested that the Mn is unlikely being reduced to metallic state. Even though TEM can show whether Mn exists as manganese oxide in both fresh and used catalysts, the oxidation state of a very small amount Mn component embedded in the metallic Rh particles cannot be decisively be justified by the experimental characterization performed in this work. It is well known that MnO bulk phase is difficult to be reduced to metallic Mn while MnO_2 is relatively easier. However, this conclusion was drawn from the reduction free energies of bulk oxide compounds [36], not the nanoclusters investigated in the present work. Since we assume the active sites for CO hydrogenation to ethanol on Rh/Mn nanoparticles, it is possible that single Mn or several Mn atom(s) surrounded by Rh atoms in the Rh-rich nanoparticles could be reduced under the reducing reaction conditions. To better understand the role of Mn as the promoter, it is essential to clarify the oxidation state Mn in which the catalytic reaction mechanism of CO hydrogenation to ethanol relies on. In order to answer this critical question, we resort to first-principles calculations.

3.2. Evidence for Rh/Mn binary alloy

To assess the oxidation state of Mn in the Rh/Mn/SiO_2 catalyst under practically operating condition, we calculated the reaction energies of the bimetallic Rh/Mn alloy particles under oxidizing conditions (CO and O_2), and the Rh/Mn oxide particles under reducing condition (H_2) using DFT. Both bimetallic Rh/Mn alloy and oxide particles were modeled by an optimized cluster model obtained from simulated annealing. Specifically, we chose the species $Rh_{50-x}Mn_x$ as our base model as it provides us with a particle on the order of 1 nm (approximately the length scale observed by TEM and XRD measurements) yet is computationally tractable with current DFT based methods. In particular, we resort to the low concentration of one and three Mn atoms to investigate both independent Mn atoms embedded in an Rh matrix as well as determine how variations in Mn surface concentration may affect the results. We noted that the following four reactions are all exothermic, indicating they are thermodynamically favorable:

$$Rh_{49}MnO + H_2 \leftrightarrow Rh_{49}Mn + H_2O, \quad \Delta H = -0.9\ \text{eV} \tag{R1}$$
$$Rh_{47}Mn_3O_3 + 3H_2 \leftrightarrow Rh_{47}Mn_3 + 3H_2O, \quad \Delta H = -0.6\ \text{eV} \tag{R2}$$
$$Rh_{49}Mn(C+O) \leftrightarrow Rh_{49}Mn(CO), \quad \Delta H = -1.0\ \text{eV} \tag{R3}$$
$$Rh_{49}Mn + 1/2O_2 \leftrightarrow Rh_{49}MnO, \quad \Delta H = -1.5\ \text{eV} \tag{R4}$$
$$Rh_{50}O + H_2 \leftrightarrow Rh_{50} + H_2O, \quad \Delta H = -0.8\ \text{eV} \tag{R5}$$
$$Rh_{50} + 1/2O_2 \leftrightarrow Rh_{50}O, \quad \Delta H = -1.7\ \text{eV} \tag{R6}$$

In reaction R3, the notation $Rh_{49}Mn(C + O)$ and $Rh_{49}Mn(CO)$ denote adsorbed atomic C and O and adsorbed CO, respectively. The equilibrium constants for these six reactions can be expressed as

$$K_1(T) = \frac{q_{Rh_{49}Mn} q_{H_2O}}{q_{Rh_{49}MnO} q_{H_2}} \tag{1}$$
$$K_2(T) = \frac{q_{Rh_{47}Mn_3}}{q_{Rh_{47}Mn_3O_3}} \left(\frac{q_{H_2O}}{q_{H_2}}\right)^3 \tag{2}$$
$$K_3(T) = \frac{q_{Rh_{49}Mn(CO)}}{q_{Rh_{49}Mn(C+O)}} \tag{3}$$
$$K_4(T) = \frac{q_{Rh_{49}MnO}}{q_{Rh_{49}Mn} q_{O_2}^{1/2}} \tag{4}$$
$$K_5(T) = \frac{q_{Rh_{50}O} q_{H_2O}}{q_{Rh_{50}O} q_{H_2}} \tag{5}$$
$$K_6(T) = \frac{q_{Rh_{50}O}}{q_{Rh_{50}} q_{O_2}^{1/2}} \tag{6}$$

where the q's are the canonical partition functions for the products and reactants. Within the harmonic approximation, the equilibrium constants for reaction (R1–R6) can be written as

$$K_1(T) = \frac{\pi^{1/2}\Theta_r^{H_2}}{T}\left(\frac{T^3}{\Theta_{r,1}^{H_2O}\Theta_{r,2}^{H_2O}\Theta_{r,3}^{H_2O}}\right)^{1/2} \frac{\prod_{j=1}^{3}\left[2\sinh\left(\frac{\Theta_{vj}^{H_2O}}{2T}\right)\right]^{-1}}{\left[2\sinh\left(\frac{\Theta_v^{H_2}}{2T}\right)\right]^{-1}} \times \exp\left[\beta\left(\varepsilon_{Rh_{49}Mn} - \varepsilon_{Rh_{49}MnO} + \varepsilon_{H_2O} - \varepsilon_{H_2}\right)\right] \tag{7}$$

$$K_2(T) = \left(\frac{\pi^{1/2}\Theta_r^{H_2}}{T}\right)^3\left(\frac{T^3}{\Theta_{r,1}^{H_2O}\Theta_{r,2}^{H_2O}\Theta_{r,3}^{H_2O}}\right)^{3/2} \frac{\prod_{j=1}^{3}\left[2\sinh\left(\frac{\Theta_{vj}^{H_2O}}{2T}\right)\right]^{-3}}{\left[2\sinh\left(\frac{\Theta_v^{H_2}}{2T}\right)\right]^{-3}} \times \exp\left[\beta\left(\varepsilon_{Rh_{47}Mn_3} - \varepsilon_{Rh_{47}Mn_3O_3} + 3\varepsilon_{H_2O} - 3\varepsilon_{H_2}\right)\right] \tag{8}$$

$$K_3(T) = \exp\left[\beta\left(\varepsilon_{Rh_{49}Mn(CO)} - \varepsilon_{Rh_{49}Mn(C+O)}\right)\right] \tag{9}$$

$$K_4(T) = 3^{-1/2}\left(\frac{2\Theta_r^{O_2}}{T}\right)^{1/2}\left[2\sinh\left(\frac{\Theta_v^{O_2}}{2T}\right)\right]^{1/2} \times \exp\left[\beta\left(\varepsilon_{Rh_{49}MnO} - \varepsilon_{Rh_{49}Mn} - 1/2\varepsilon_{O_2}\right)\right] \tag{10}$$

$$K_5(T) = \frac{\pi^{1/2}\Theta_r^{H_2}}{T}\left(\frac{T^3}{\Theta_{r,1}^{H_2O}\Theta_{r,2}^{H_2O}\Theta_{r,3}^{H_2O}}\right)^{1/2} \frac{\prod_{j=1}^{3}\left[2\sinh\left(\frac{\Theta_{vj}^{H_2O}}{2T}\right)\right]^{-1}}{\left[2\sinh\left(\frac{\Theta_v^{H_2}}{2T}\right)\right]^{-1}} \times \exp\left[\beta\left(\varepsilon_{Rh_{50}} - \varepsilon_{Rh_{50}O} + \varepsilon_{H_2O} - \varepsilon_{H_2}\right)\right] \tag{11}$$

$$K_6(T) = 3^{-1/2}\left(\frac{2\Theta_r^{O_2}}{T}\right)^{1/2}\left[2\sinh\left(\frac{\Theta_v^{O_2}}{2T}\right)\right]^{1/2} \times \exp\left[\beta\left(\varepsilon_{Rh_{50}O} - \varepsilon_{Rh_{50}} - 1/2\varepsilon_{O_2}\right)\right] \tag{12}$$

where Θ_r are the rotational temperatures, Θ_v are the vibrational temperatures, $\beta = 1/k_BT$, and ε are the ground state energies determined from our DFT calculations. The rotational and vibrational temperatures for the various species were obtained from statistical mechanics [37]. Note that the vibrational and rotational contributions to the partition functions in reaction R3 have not been included as their ratio is expected to very close to unity. Fig. 5 shows the equilibrium constants $K(T)$ for reactions R1–R6 in the

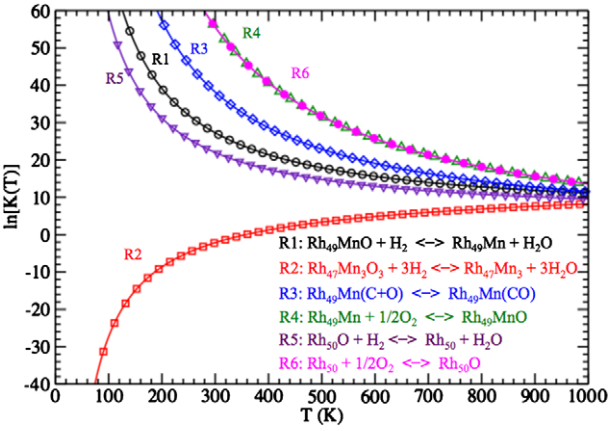

Fig. 5. Calculated equilibrium constants $K(T)$ for the reactions R1–R6 as a function of temperature.

temperature range of 0–1000 K. In the relevant experimental temperature range of 400–700 K, the equilibrium constants clearly indicate that the binary Rh/Mn alloys are favored over the Rh/Mn oxides (black and red curves), and that the reformation of adsorbed CO is preferred over adsorbed C and O atoms (blue curve). This is in contrast to the previous assumption that the separate metallic Rh and MnO phases were co-existed considered in the $Rh/Mn/SiO_2$ catalysts [14]. On the other hand, Fig. 5 shows that the equilibrium constants for the oxidation reactions (R4 in green curve and R6 in magenta curve) favors the oxide under ambient oxygen partial pressure (P_{O2} = 0.21 atm). This suggests that although the supported Rh/Mn particles might be reoxidized under the ambient condition in the characterization. We believe that the $Rh/Mn/SiO_2$ catalyst would prefer to be a binary metal alloys supported on silica under operating reaction conditions where the high temperatures and reducing atmosphere prevail.

Our thermodynamical analysis suggests that a binary Rh/Mn alloy nanoparticle may be the phase form of the active $Rh/Mn/SiO_2$ catalyst under *in situ* reaction conditions. Moreover, our analysis also indicates that characterization of the catalyst particles, once exposed to oxygen, yields an interpretation of Mn in an oxide state. This may be the reason why the previous spectroscopic studies suggested that only Mn oxides were identified [8,14,20,38,39]. Further theoretical calculations for larger Rh/Mn particle systems, as well as the consideration of anharmonic effects on the free energy difference will be needed to confirm this conclusion. For the purposes of the current study, we will focus on how the presence of Rh/Mn binary alloy influences the chemical reactivity of the conversion of syngas to ethanol.

3.3. Catalytic performance

Experimental kinetics including the selectivities and STYs of methanol, C_2^+ alcohols, other C_2^+ oxygenates, methane, C_2^+ hydrocarbons are given in Table 1. We found that methane selectivity is high, about 30–60%, depending upon the temperature and the space velocity. Typically, the selectivity of hydrocarbon, C_2^+ oxygenates, and C_2^+ alcohols is 10–25%, 20–40%, and ~10% respectively. The total CO conversion ranges from 6% to 60%. In these experiments, no significant conversion of CO to CO_2 via water gas shift reaction was found.

As expected, CO conversion generally increases with temperature but decreases with the GHSV. While the STYs increases with the increasing temperature up to about 300 °C, there appears to be a decrease in the activity of the catalyst at 315 °C or higher. Increasing the GHSV, the CO conversion reduces while the STY remains the same, suggesting an overall deactivation of the catalyst at higher temperatures. The repeating experiments under the same pressure and the GHSV at lower temperatures confirm this conclusion. Although with some fluctuations, our results show the selectivity to C_2^+ oxygenates decreases while the selectivity to C_2^+ alcohols increases with increasing temperature. Similarly, the carbon selectivity to hydrocarbon liquids is eliminated and to higher hydrocarbon gases (ethane, propane, etc.) is significantly reduced as the catalyst is deactivated. This is illustrated in Table 1 by the reduced production of other hydrocarbons in the experiments conducted after 317 °C, suggesting a deactivation of the catalyst due to hydrocarbon chain growth process on the catalyst. Herein, the most relevant experimental observation is the selectivity of methane increases, while the selectivity to C_2^+ oxygenates and alcohols decreases as the temperature increases.

4. Theoretical and kinetic modeling

4.1. Reaction network

To understand how the promoters affect the reactivity and the selectivity of CO hydrogenation to ethanol over the Rh-based catalysts, a comprehensive reaction mechanism network which is based on previous theoretical and experimental studies [1–3,5,6,8–10,13,14,17–19] was built. As shown in Fig. 1, the reaction mechanism network for CO hydrogenation to ethanol used in the simulations is very complex even though we do not include some of the "side" reaction routes such as methanol homologation, methanol condensation/coupling that had been found to be the major reaction routes on CuO-based catalysts [5,6]. We have

Table 1
Experimental results of CO hydrogenation over $Rh/Mn/SiO_2$ catalyst.

Test conditions			Carbon selectivity (C-mol%)					STY ($g/mL_{cat}/h$)				
Space velocity ($L/L_{cat}/h$)	Temp. (°C)	CO conv. (%)	Methanol	C^{2+} alcohols	Other C^{2+} oxygenates	CH_4	Other HCs	C^{2+} alcohols	Other C^{2+} oxygenates	Total C^{2+} oxygenates	Methanol	Total organic liquids
7500	256	6.67	0.48	7.85	30.46	36.98	24.22	0.01	0.06	0.07	0.00	0.08
7500	277	20.78	0.50	8.35	43.24	31.71	16.21	0.04	0.23	0.28	0.00	0.29
11,000	300	26.37	0.41	9.10	32.31	39.21	18.96	0.09	0.33	0.42	0.01	0.46
11,000	317	41.50	0.37	8.66	25.84	46.71	18.41	0.13	0.31	0.44	0.01	0.46
11,000	314	31.56	0.34	9.12	22.59	53.65	14.30	0.10	0.33	0.43	0.01	0.45
11,000	324	37.24	0.34	9.25	22.90	55.19	12.32	0.12	0.32	0.44	0.01	0.45
15,000	324	26.36	0.51	9.41	19.41	59.76	10.91	0.12	0.26	0.37	0.01	0.38
15,000	315	23.09	0.68	9.67	25.01	52.16	12.48	0.11	0.29	0.40	0.01	0.41
15,000	302	13.32	0.85	9.40	25.87	52.93	10.95	0.06	0.18	0.24	0.01	0.24
11,000	302	20.54	0.87	10.16	29.49	47.06	12.41	0.07	0.23	0.31	0.01	0.31
7500	256	2.62	1.50	12.42	21.86	61.09	3.12	0.01	0.02	0.02	0.00	0.02

chosen to neglect these steps in order to simplify the parameterization of our model without loss of any of the most important reaction product channels. A total of 230 elementary steps that lead to a variety of products from CO hydrogenation are implemented in our first-principles-based kinetic Monte Carlo simulations.

Herein, we only give a brief description of the catalytic conversion of CO hydrogenation to ethanol. Generally, the reaction begins with the associative adsorption of CO and the dissociative adsorption of H_2. CO molecules adsorb at all surface sites (atop, bridge, 4-fold hollow, and 3-fold hollow) of both (1 0 0) and (1 1 1) facets [40,41]. The adsorbed atomic H preferentially occupies either bridge sites or hollow sites on both facets. Adsorbed CO can further dissociate into atomic C and O that prefer to sit on the hollow sites of both facets [42,43]. The C and H atoms recombine to form CH and further hydrogenation with the surface H atoms forming CH_2 and CH_3, and the major side product CH_4. These CH_x intermediates can also couple themselves producing higher hydrocarbons [40,44–48]. In this work, only C_2 hydrocarbons are considered for simplifying the reaction mechanism. The key elementary steps for CO hydrogenation to ethanol are the insertion of CO into the CH_x (x = 1–3) species forming CH_xCO species [17]. This is also in accord with in recent theoretical study that CH_3 + CO is the key step for ethanol synthesis on Rh(1 1 1) [21]. The desired ethanol product will be generated by further hydrogenation of CH_xCO. Meanwhile, the intermediate CH_xCO species will also be oxidized and hydrogenated to form other C_2 oxygenates such as acetaldehyde, acetic acid, and ethyl acetate [17] shown in Fig. 1. The adsorption structures for the CH_xCO species are shown in Fig. 6. On the other hand, the hydrogenation of adsorbed CO can form formyl (HCO) or COH species. HCO (or COH) intermediates are then assumed to be hydrogenated into methanol as the major product from CO hydrogenation [21,49].

4.2. Kinetics parameter database

Since the entire reaction network consists of a large number of elementary steps, it would be impractical to calculate all the energetics including adsorption energies of the reactive species, the reaction energies and activation barriers of each elementary step. As a result, we only calculated the binding energies of the major reaction intermediates, as well as the reaction energies and activation barriers of the insertion reactions of CO + CH_x and methanation reaction on the Rh and Rh/Mn nanoparticles using DFT methods. The DFT-based energetics are then used as database to estimate other energetics using the semi-empirical UBI-QEP method [25,44,50,51]. Also some of the energetics was taken for the literature [40,42,43,45–48,52–61]. The entire energetic database used in the KMC simulations will be given in the Supplementary material. Since we are focusing on the qualitative description of the reaction kinetics of CO hydrogenation to ethanol, we believe the accuracy of the energetics for the crucial elementary steps of the entire reaction mechanism network will be enough to capture the chemistry of ethanol synthesis from CO hydrogenation.

Instead of using periodic slab surface as the catalyst model, the Rh and Rh/Mn nanoparticles catalysts that derived from aforementioned experimental characterization were modeled as Rh_{50}, $Rh_{49}Mn$, $Rh_{47}Mn_3$ clusters in this work. The Mn compositions used in the model Rh/Mn nanoparticles are justified against the experimental compositions observed for the mixed Rh/Mn nanoparticles (see experimental section). For example, there is one Mn atom (three Mn atoms) surrounded by nine (or six) Rh atoms in our $Rh_{49}Mn$, $Rh_{47}Mn_3$ model clusters. Thus, the Mn surface composition is about 10% for $Rh_{49}Mn$ and 33% for $Rh_{47}Mn_3$ particles. This is in the range of experimental measured compositions with ~13% and ~42% atomic Mn in the Rh/Mn sample (S3, see Fig. 3) before and after the reaction. We found that the internal Mn atoms of Rh/Mn nanoparticles have a very minor influence on the energetics and kinetics of the reactions we calculated in the present work. In the calculations, adsorbates molecules were put on the cluster at a quasi-(1 1 1) surface facet, so that the binding metal sites have similar local coordination to the bulk surface in order to mimic the local coordination environment of larger bulk-like particles. Moreover, for large bulk-like transition metal particles, the (1 1 1) surface is the most stable structure due to its low surface energy. The calculated binding energies of the major surface intermediates on the Rh_{50}, $Rh_{49}Mn$, $Rh_{47}Mn_3$ clusters are given in Table 2. Fig. 6 shows the adsorption configurations of some of these surface intermediate species on the $Rh_{47}Mn_3$ cluster. The binding energies of other surface intermediates were estimated by UBI-QEP method [25] using the calculated DFT values of C, O, and H as the basis.

As we mentioned earlier, first-principles DFT calculations performed in this work focused on the reaction energetics of the most important steps in the catalytic CO hydrogenation mechanism and their dependence upon the promoter identity. Previous experiments suggested that methane is a major side product (over 50% of all products) in CO hydrogenation over Rh-based catalysts [7–13]. To improve the selectivity to ethanol, different promoters were added to Rh catalysts to control the reaction routes to either methanation or CO insertion to CH_x leading to ethanol and other C_2 oxygenates [5,6]. To this end, we investigated methane formation against CO addition into CH_x on the Rh_{50}, $Rh_{49}Mn$, $Rh_{47}Mn_3$ nanoparticles using DFT and CI-NEB methods [34,35] at the same theoretical level. All atoms were optimized to the energy minima without constraints on any component of the molecular geometry.

We first calculated the reaction path $CH_3 + H \rightarrow CH_4$, which is the final hydrogenation step for methane formation on the Rh_{50}, $Rh_{49}Mn$, $Rh_{47}Mn_3$ nanoparticles. As shown in Fig. 7, methane formation is exothermic on Rh_{50} and $Rh_{49}Mn$ clusters while it is slightly endothermic on $Rh_{47}Mn_3$. This indicates that methane formation is thermodynamically more favorable than methane dissociation on Rh and Rh/Mn nanoparticles. The calculated reaction energies of $CH_3 + H \rightarrow CH_4$ on Rh_{50}, $Rh_{49}Mn$, and $Rh_{47}Mn_3$ are −0.36, −0.22, +0.08 eV, respectively. The calculated activation barrier for $CH_3 + H \rightarrow CH_4$ is 0.60 eV on the Rh_{50} cluster, which is in agreement with to the previously reported barriers of 0.65 eV [55]; 0.63 eV [45] on Rh(1 1 1). By doping one Mn atom on the surface of the Rh_{50} cluster ($Rh_{49}Mn$), the barrier for methane formation increases slightly to 0.70 eV. If three Mn atoms are doped onto the Rh_{50} cluster ($Rh_{47}Mn_3$), this barrier only slightly decreases to 0.57 eV. This implies that doping Mn into Rh nanoparticle essentially does not change the activation barrier of methane formation. Considering the other hydrogenation steps of CH_x (where x = 0–2) on Rh(1 1 1) have the similar low barriers between 0.47 and 0.69 eV [47,48,54,55], we can expect that the methane formation is still inevitable in CO hydrogenation by adding Mn into Rh catalyst. In other words, the addition of Mn into Rh has little effect on the catalytic performance with respect to the methane formation since both the thermodynamical and kinetic factors for the hydrogenation of CH_x are nearly the same for Rh and Rh/Mn catalysts. This conclusion is also supported by our experimental results. As shown in Table 1, the methane selectivities on Rh/Mn/SiO_2 under different experimental conditions are still high (~31–60%). Previous experimental investigations of CO hydrogenation on the Mn promoted Rh catalysts showed the similar results of high methane selectivities [13,14,16,20,38,62,63]. For example, Hu et al. observed that the methane selectivities are in the range of 34–54% [62]. Ojeta et al. found the methane selectivity increased from 22% to 32% as the reaction temperature increased from 240 to 260 °C [38].

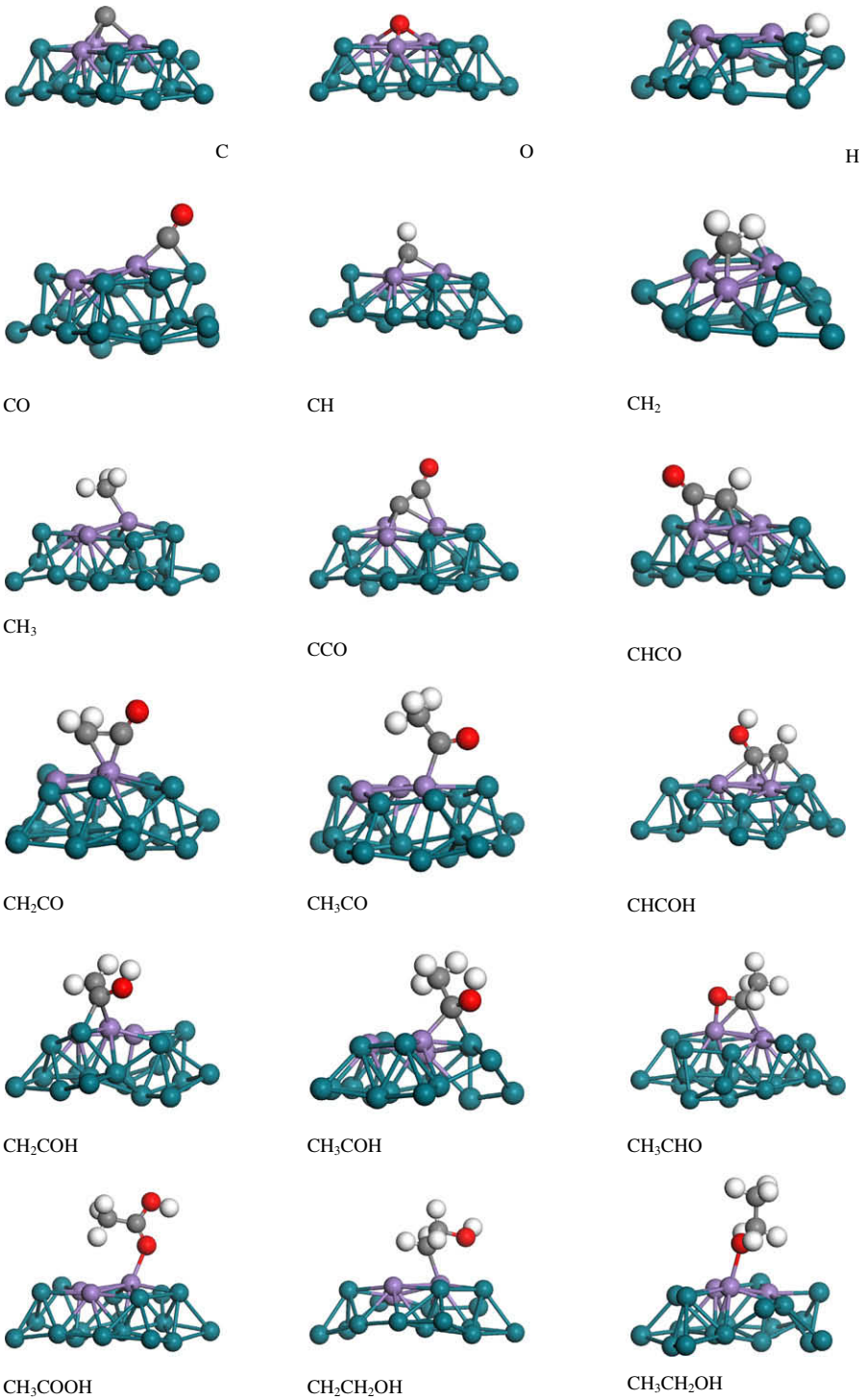

Fig. 6. The optimized configurations of the key surface reaction intermediates on $Rh_{47}Mn_3$ alloy nanoparticle. Rh in dark green; Mn in purple; O in red; C in gray; and H in white. (For interpretation of the references to color in this figure legend, the reader is referred to the web version of this article.)

In order to form C_2^+ oxygenates by CO hydrogenation, the CO insertion step is vital. Noting that the hydrogenation of CH_x ($x = 0$–3) species is facile due to the low barriers. The CO insertion process can only be kinetically feasible if the barriers are lower than, or at least comparable to, the barriers for CH_x hydrogenation. To understand whether the addition of Mn into Rh would affect the CO insertion reaction into CH_x species, we explored the energetics of four possible CO insertion reactions on the Rh_{50}, $Rh_{49}Mn$, $Rh_{47}Mn_3$ nanoparticles:

$$C + CO \rightarrow CCO \quad (R7)$$

$$HC + CO \rightarrow HC - CO \quad (R8)$$

$$H_2C + CO \rightarrow H_2C - CO \quad (R9)$$

$$H_3C + CO \rightarrow H_3C - CO \quad (R10)$$

For the reaction R7, our calculations show that the activation barriers are on the order of 2 eV over all the catalyst particles studies here. This is due to the fact that the bare C atom forms a very strong bond with surface Rh atom. The binding energy of C atom

Table 2
DFT calculated binding energies (in eV) of the surface intermediates on pure Rh, and the Rh/Mn alloy nanoparticles.

Surface intermediate	Site	Bind energies (eV)		
		Rh_{50}	$Rh_{49}Mn$	$Rh_{47}Mn_3$
H	3-Fold fcc	−0.62	−1.15	−1.35
C	3-Fold fcc	−6.58	−6.34	−6.21
O	3-fold fcc	−3.32	−3.22	−3.16
CO	3-Fold fcc	−1.68	−2.42	−1.74
CH	3-Fold fcc	−6.19	−4.94	−5.82
CH_2	3-Fold fcc	−3.42	−4.21	−5.30
CH_3	Top	−1.11	−2.96	−3.91
CH_4	Top	−0.09	na	na
CCO	3-Fold fcc	−5.11	−4.29	−4.11
CHCO	3-Fold fcc	−3.37	−3.21	−3.14
CH_2CO	Top	−1.18	−1.33	−1.22
CH_3CO	Top	−1.89	−1.73	−1.54
CHCOH	2-Fold bridge	−3.68	−2.93	−3.34
CH_2COH	2-Fold bridge	−2.82	−3.06	−3.35
CH_3COH	2-Fold bridge	−4.04	−2.78	−3.52
CH_3CHO	2-Fold bridge	−1.41	−1.32	−1.25
CH_3COOH	Top	−0.72	−0.36	−1.00
CH_2CH_2OH	Top	−1.65	−1.15	−1.65
CH_3CH_2OH	Top	−0.93	−0.67	−1.01

Note: "na" indicates a non-adsorption state.

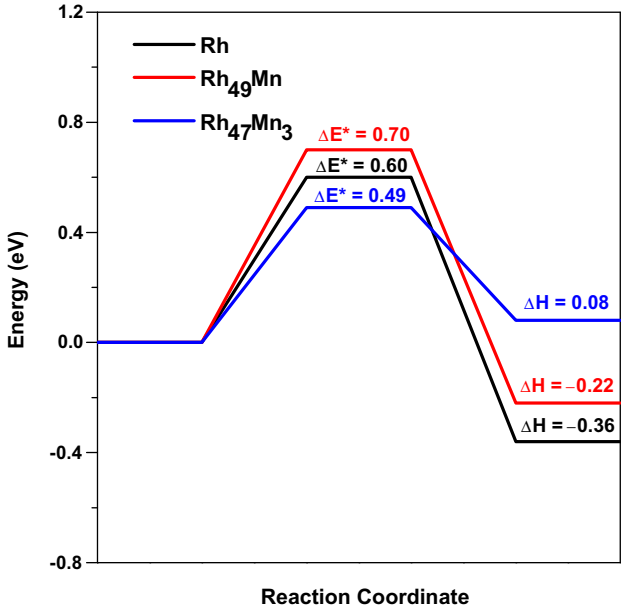

Fig. 7. DFT calculated reaction energies and activation barriers of $CH_3 + H \leftrightarrow CH_4$ on the Rh, $Rh_{49}Mn$, and $Rh_{47}Mn_3$ particles.

is −6.54 eV on the Rh_{50} and −6.28 eV on the $Rh_{49}Mn$ nanoparticles. Therefore, we can safely disregard the C + CO coupling reaction as having a strong influence on the reaction kinetics. Fig. 8a compares the reaction energies and activation barriers of CH + CO reaction. Unlike the methane formation, this step is endothermic for the Rh_{50} and the $Rh_{49}Mn$ and almost neutral for the $Rh_{47}Mn_3$, indicating that insertion of CO into CH species is not thermodynamically favorable on pure Rh_{50} and $Rh_{49}Mn$ nanoparticles. For the Rh_{50} particle, the activation barrier of this reaction is 1.35 eV. However, we found that doping Mn into Rh dramatically lowers the insertion barriers to only 0.69 for the $Rh_{49}Mn$ and 0.58 eV for the $Rh_{47}Mn_3$. The lower CO insertion barriers may be caused by the tilted CO adsorption configuration on the $Rh_{49}Mn$ and $Rh_{47}Mn_3$ particles. With addition of Mn, CO adsorbed at 3-fold hollow site with an upright configuration on Rh_{50} shifts to atop or 2-fold bridging Rh sites with a tilted configuration toward to Mn, which is consistent with previous experimental observations [19,24] that the tilted CO plays an important role in CO insertion reaction. As a consequence, CO insertion into CH reaction becomes competing step with the methane formation on the $Rh_{49}Mn$ and $Rh_{47}Mn_3$ particles. We also noted that since the reaction energy of CH + CO is 0.52 eV, the formed CHCO on the $Rh_{49}Mn$ could easily dissociate back to CH and CO with a barrier of 0.17 eV. As such, only the $Rh_{47}Mn_3$ particle provides a feasible promoting path for CO insertion into CH comparing with the pure Rh_{50} nanoparticle. This latter observation indicates that although Mn sites alone do help in lowering the barrier to the formation of CHCO they are most effective when clustered, as in $Rh_{47}Mn_3$ indicating that reasonably high concentrations of Mn in the proposed Rh/Mn alloy are required.

The calculated reaction energies and activation barriers of the reaction R9 on the Rh_{50}, $Rh_{49}Mn$, $Rh_{47}Mn_3$ nanoparticles are shown in Fig. 8b. On pure Rh nanoparticles, the barrier is found to be about 1.5 eV and is only marginally lower by about 0.2–0.3 eV by inclusion of Mn into the nanoparticle. It is surprising that this insertion step is found to be highly endothermic with high barriers on all the particles, indicating the insertion of CO into the surface CH_2 species is difficult. Likewise, insertion of CO into CH_3 with R10 reaction on different Rh-based nanoparticles is shown in Fig. 8c where it is also found that the activation barriers of this step are still high, about 1.0–1.26 eV, although this step is nearly energy neutral for all catalyst nanoparticles. Our calculated barrier of 1.07 eV for CH_3 + CO path is in good agreement with recent reported value of 1.15 eV on Rh(1 1 1) [21]. Compared with to the barriers of 0.5–0.7 eV for methane formation, it is expected that the insertion of CO to CH_2 and CH_3 is still kinetically inhibited even with the addition of Mn into Rh. This also explains why methane is still the dominant side product in CO hydrogenation for the Rh/Mn catalysts.

It is noteworthy that different CO insertion pathways occur on the Rh and Rh/Mn catalysts based on our calculations. On the pure Rh, CO + CH_3 reaction is kinetically more favorable than other two CO insertion paths (CO + CH and CO + CH_2). Although the barrier for CO + CH_3 insertion is only 0.1 eV lower than the barrier of CO + CH coupling, however, the reaction energies of these two reactions are very different. The CO + CH is almost highly endothermic (1.31 eV) while the CO + CH_3 path is only slightly endothermic (0.30 eV). Consequently, the formed CHCO species will immediately dissociate back to co-adsorbed CO and CH species with almost no barrier. On the other hand, the barrier for the dissociation of the formed CH_3CO species is 0.96 eV. As a result, the CH_3CO species could remain on the Rh catalyst particle for further hydrogenation to other C_2^+ oxygenates. This is consistent with the previous experimental spectroscopic evidences that acyl (CH_3CO) is the key reaction intermediate leading to C_2^+ oxygenates during CO hydrogenation on Rh catalyst [17,19]. For the Rh/Mn catalysts, the three CO insertion paths shown in Fig. 8 clearly indicate that CO + CH path is the preferential pathway for CO insertion steps. As a result, the CHCO instead of CH_3CO becomes the vital reaction intermediate to the formation of C_2^+ oxygenates.

In summary, our DFT results suggest that the promoting effect of doping Mn into Rh catalysts for CO hydrogenation to ethanol that the higher selectivity to C_2^+ oxygenates observed in the previous experiments [13,14,16,20,38,62,63] is due to enhancement of the CO insertion step via CH + CO → CHCO reaction. This reaction channel is expected to be competitive with the hydrogenation of CH to form CH_2 or CH_3, estimated based on DFT calculations to require and activation energy on the order of 0.5–1.0 eV, or dehydrogenation to form C at an energetic cost of about 1.0 eV [45]. Hence, our results suggest that by adding the Mn component into Rh cat-

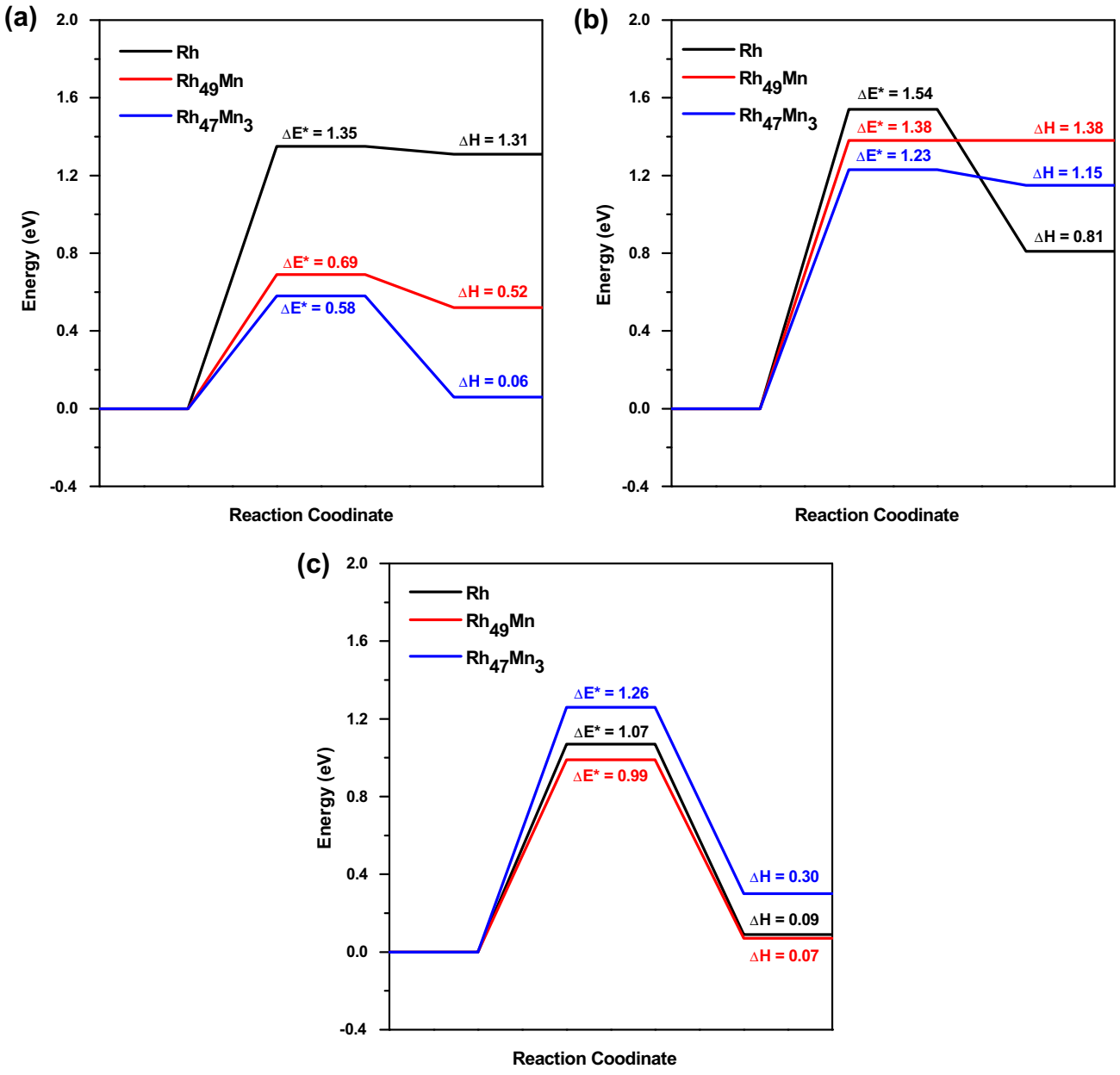

Fig. 8. DFT calculated reaction energies and activation barriers of CO insertion into CH_x on the Rh, $Rh_{49}Mn$, and $Rh_{47}Mn_3$ particles. (a) $CO + CH \leftrightarrow CHCO$; (b) $CO + CH_2 \leftrightarrow CH_2CO$; (c) $CO + CH_3 \leftrightarrow CH_3CO$.

alysts, the activation barrier for CO insertion into CH forming CHCO species is low enough to compete with the dominant methanation reaction paths. On the other hand, our calculations indicate that the methane formation is largely unaffected by Mn doping and is thus still a main reaction channel on Rh/Mn catalysts [13]. One can thus conceptualize this process as the dopant providing an energetic route for stealing, but not completely diverting, reactive flux from the methanation channel to form C_2^+ oxygenates.

4.3. Kinetic Monte Carlo simulation

In order to understand how various promoters affect the catalytic performance on Rh-based catalysts, a working kinetic reaction model that describes CO hydrogenation over supported Rh nanoparticle catalyst, we build a detailed kinetic Monte Carlo (KMC) simulation model with our calculated DFT data as well as literature database as the input. We have performed a series of KMC simulations to validate our model by comparing calculation results against experimental catalytic reaction kinetics of CO hydrogenation over the $Rh/Mn/SiO_2$ catalysts under the operating conditions. The validation of KMC model presented in this work will be very useful in the computational screening of different promoters added to Rh catalysts to improve the catalytic performance, especially for improving the selectivity to C_2^+ oxygenates and preventing the methane formation. We first discuss the structure of supported Rh/Mn catalyst particle used in the simulations and how the available reaction sites influence the chemistry and then report our results of how the various thermodynamics variables such as pressure temperature and promoter concentration influence catalyst activity.

4.3.1. Three-dimension supported catalyst nanoparticle model

The geometric shape and exposed facets (crystal planes) of supported metal nanoparticles depend on many factors such as the

size of the particle, the supporting materials, the preparation method, and *in situ* reaction conditions. The equilibrium shape of a free metal particle (without support) is generally determined by the Wulff rule: the shape of the metal particle is determined by minimizing the surface energy of the particle. As the particle size becomes greater than 2 nm, the shape of the particles and the nature of facets can be experimentally explored by electron microscopy techniques such as high-resolution TEM, XPS, and XRD. For Rh-based bimetallic nanoparticles, the most common shape is the cubo-octahedral structure consisting of (1 1 1) and (1 0 0) facets, where the (1 1 1) facet dominates the surface of the nanoparticle [64]. However, the nanoparticle shape is subject to change under reaction conditions or after high temperature pretreatment. It had been observed that the Rh-based nanoparticle shape changed from a cubo-octahedral in the reducing reaction environment to a more spherical shape in an oxidizing environment [64]. Since CO hydrogenation reaction is operating at the reducing environment, a three-dimensional model with truncated octahedral nanoparticle structure is used to represent the SiO_2 supported Rh/Mn catalytic nanoparticle in this work. The truncated octahedral nanoparticle, shown in Fig. 9, has eight (1 1 1) facets and one (1 0 0) facet. The relevant experimental characteristics included in this model are as follows: (1) both (1 0 0) and (1 1 1) facets covering the nanoparticle surface; (2) the (1 1 1) facet dominates the nanoparticle surface; (3) the nanoparticle is nearly spherical in the case of more oxygenates produced in the reaction process. We neglect any shape transformation and surface reconstruction that may be induced by reactant adsorption or the evolution of the surface intermediates during the reaction. The size of Rh/Mn nanoparticle is represented by the total number of atoms along with widest side (L) and the total number of height layers (H). As shown in Fig. 9, the Rh-based catalyst nanoparticle with 30% Mn (Rh/Mn atomic ratio = 7:3) is designated by size as $L \times H = 12 \times 7$. The total number of atoms and numbers of Rh and Mn atoms in the Rh/Mn nanoparticle are 748, 673, and 75, respectively. The numbers of surface atoms and bulk atoms of the Rh/Mn nanoparticle are 309 and 439, in which the number of atoms on the (1 0 0) and the (1 1 1) facets, and the number of atoms on edge and corner sites of the model Rh/Mn nanoparticles are 49, 136, 112, and 12, respectively. The diameter of the model nanoparticle, $D_{particle}$, is determined by the following equation based on the spherical particle assumption:

$$D_{particle} = d_{atom} \times N_{total}^{1/3} \tag{9}$$

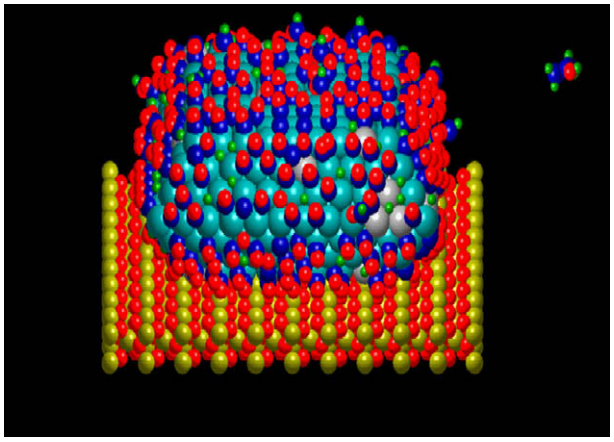

Fig. 9. Snapshot of KMC simulation of CO hydrogenation to ethanol over the three-dimensional Rh/Mn/SiO_2 catalyst nanoparticle. Rh in light blue; Mn in silver; C in blue; O in red, H in green; and Si in yellow. (For interpretation of the references to color in this figure legend, the reader is referred to the web version of this article.)

where d_{atom} is the diameter of Rh atom (0.269 nm), and N_{total} is the total number of atoms in the nanoparticle. As a result, the diameter of the three-dimensional Rh/Mn nanoparticle used in this work is about 2.44 nm. This model catalyst size is close to the used Rh/Mn catalyst measured by TEM (~3 nm). The surface composition and actual surface position of Mn atoms in the simulated Rh/Mn nanoparticle are changed during the reaction. These changes depend on the segregation surface energies, and also depend on the adsorption energies of adsorbates that were calculated by DFT [65–67]. Since we do not have enough kinetics parameters to accurately describe these changes, only thermodynamic factors are considered in our simulations. Due to the major effect of Mn is that it lowers the barrier toward CO insertion and is an electronic effect. Ensemble effects included in the KMC model do not significantly enhance or inhibit kinetics and hence play only a minor role. The effect of silica support on the reaction kinetics has not been considered due to the lack of kinetic parameters on silica and on the interface between silica and the supported Rh/Mn nanoparticle.

4.3.2. KMC approach

The details of the KMC algorithm have been extensively described in previous publications [68–71]. A brief description of this approach is given in the next paragraph. The structural, electronic, and energetic properties calculated from DFT for the intermediates were used as input parameters of the simulation. This includes the binding energies and molecular structures of the adsorbates at all possible adsorption sites, van der Waals radii (physical size) for all of the reactants, the intermediates and products along with the reaction energies and activation barriers for elementary surface kinetic processes. This intrinsic kinetic database is subsequently combined with the lateral interaction models and incorporated into the core reaction kinetics model in the KMC simulation. After initialization, all the sites on the particle surface are stochastically screened in order to construct a cumulative reaction probability distribution that outlines all the possible surface events used in the model. This includes adsorption, surface reaction, surface and inter-facet diffusion, and desorption. These surface events are considered to be dependent on the specific characteristic of the active site of the event and its surrounding reaction environment. The active sites on the particle surface include sites on the top (1 0 0) facet, eight side (1 1 1) facets, and four edge (1 1 1)/(1 0 0) boundaries. We treated the edge (1 1 1)/(1 1 1) boundary sites and four (1 1 1)/(1 0 0)/(1 1 1) corner sites as reaction-free sites. Diffusion only occurs on the (1 0 0) and (1 1 1) facets. The edge (1 1 1)/(1 0 0) boundaries are treated as the (2 1 1)-like structure where only CO dissociation occurs. The barrier for CO dissociation on the edge (1 1 1)/(1 0 0) boundaries used in our KMC simulations is 0.3 eV, which is taken from previous DFT calculations of CO dissociation on stepped sites over Rh(2 1 1) [55]. We also note that a very high activation barrier of ~2 eV for CO dissociation on Rh(2 1 1) was reported by Mavrikakis et al. [72]. Since CO dissociation would not occur on low-index Rh surfaces such as the (1 1 1) and the (1 0 0) facets [73], we found that there is almost no activity for ethanol formation under the operating conditions if the barrier of ~2 eV for CO dissociation was used in our KMC simulations. This is inconsistent with our experimental observations. Therefore, we chose the low barrier of 0.3 eV for CO dissociation in the simulations. Correspondingly, a scaled barrier of 0.25 eV for CO dissociation on Rh/Mn catalysts was used in this study. For each surface reaction event, we calculated the binding energies of reactants and the possible products on the reactive sites for both initial configuration states and final configuration states. The effects of local reaction environment on the energetics are included in the simulations by using the lateral interaction models described in previously published work [68–71,74–77]. At any instant in time t_i, the rates for all possible events over the entire particle surface

are added up to determine the total reaction rate. The total reaction rate is subsequently used along with the variable time step algorithm to determine the time at which the possible event on the surface occurs. The specific reaction that occurs within the calculated time step interval is chosen based on the cumulative reaction probability distribution. The particle surface is updated accordingly based on this chosen surface event. The rate constant for each elementary step r_i is calculated using transition state theory:

$$r_i = \nu_i \exp[-\beta \Delta E_i^*] \tag{10}$$

where ν_i is the pre-exponential factor, T is the temperature, and ΔE_i^* is the activation energy barrier for this elementary reaction i. We assume that the activation energy barrier is equal to the difference of the electronic energies of the reactant ground state and the transition state, and thus neglect the zero-point energy effects. Along with the reaction barriers of CO + CH_x coupling and methanation on the Rh/Mn(1 1 1) surfaces we have discussed in the aforementioned section, the activation barriers of other elementary surface reaction steps in the reaction network have been estimated using the UBI-QEP method [25] (see the supporting information). The diffusion barrier for the adsorbate is assumed to the difference of the binding energies of the adsorbate at the two stable sites. The preexponential frequency factors, ν_i, were chosen to be consistent with statistical mechanical estimates, and thus we assume 10^{13} s^{-1} for elementary surface reaction and diffusion steps [68,70,71]. The adsorption rate constant for species i is given by:

$$r_{ad,i} = \frac{s_o P_i A_s}{\sqrt{2\pi m_i k_B T}} \exp[-\beta \Delta E_i^*] \tag{11}$$

where s_o is the sticking coefficient, P_i is the partial pressure of species i, A_s is the area of one surface site, and m_i is the molecular mass of species i. The sticking coefficients of CO on the (1 0 0) and (1 1 1) facets are taken to be 0.7 and 0.6, respectively [41,78]. The sticking coefficients of H_2 on the (1 0 0) and (1 1 1) facet are taken to be 0.8 and 0.2 based on experimental measurements [78,79].

Each simulation was allowed to equilibrate to a steady state in which the surface coverage for all of surface intermediates reached constant values, with the exception of small fluctuations resulting from the stochastic nature of the simulation. After achieving the steady state, the overall macroscopic kinetic values, such as the turnover frequencies (TOFs) of the major products and averaged surface coverages for the key surface intermediates were calculated. For example, the TOF for ethanol production was calculated by simply counting the number of ethanol molecules desorbing from the Rh/Mn nanoparticle surface during a given time interval. The number of molecular desorption events as a function of time was fitted to a simple function that includes a first-order exponential term to describe the initial transient kinetics, followed by a straight line to model the long-time steady-state behavior. The TOF values reported herein were determined from the long-time behavior, in which the slope of the straight line was normalized based on the total number of surface Rh/Mn atoms on the nanoparticle. The time scale of the simulations vary depending on the specific conditions, but the steady state is typically realized somewhere between 0.01 and 10.0 s.

4.3.3. Simulation results and discussion

KMC simulations can be used to track actual catalytic chemical transformations over the well-defined model catalysts at the experimental operating conditions. We carried out KMC simulations of CO hydrogenation to ethanol over silica supported three-dimensional Rh/Mn catalytic nanoparticles with an atomic bulk composition of 30% Mn as suggested by experimental characterization. The partial pressures of CO and H_2 in the gas phase were set to be 0.67 and 1.33 MPa, respectively. The temperature range examined here varies from 227 to 427 °C, which is slightly larger than our experimental temperature range. Methane, acetaldehyde and ethanol are found to be the three major products for CO hydrogenation over the Rh/Mn/SiO_2 catalyst. Other products such as acetic acid, methanol, and ethane are relatively minor. Fig. 10 shows the TOFs for ethanol, methanol, methane, acetaldehyde, and acetic acid formation increase with the increasing temperature. The apparent activation energy for ethanol formation is 37 kcal/mol which is in good agreement with the reported experimental measurement of 45 kcal/mol under the similar operating conditions [11]. Similarly, the apparent activation energies of methane, acetaldehyde, and acetic acid are 35, 24, and 12 kcal/mol, respectively also in agreement with previously reported data of 34, 19, and 7.5 kcal/mol, respectively [11]. Thus, our kinetic model at least semi-qualitatively reproduced the apparent activation energies of the major species with the correct energy ordering.

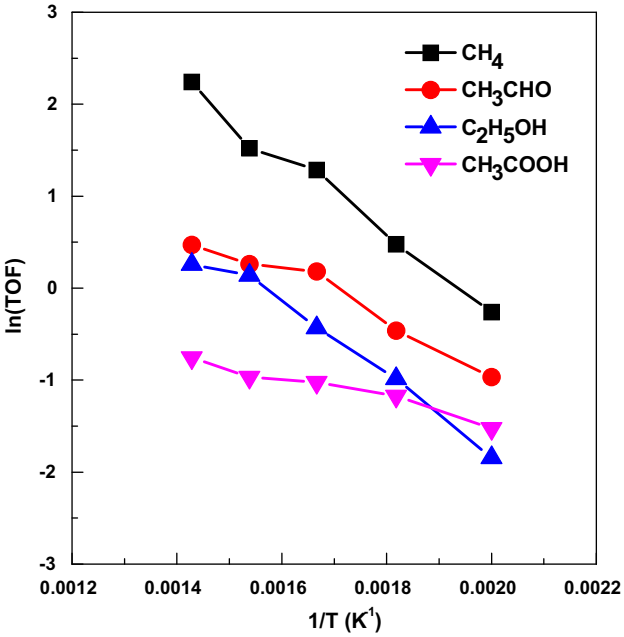

Fig. 10. The temperature dependence of TOFs of major products from CO hydrogenation over the Rh/Mn/SiO_2 catalyst at P = 2.0 MPa (P_{CO}/P_{H2} = 1:2).

The selectivity to each of the five products is defined as

$$S_i = \frac{TOF_{product(i)}}{TOF_{all\ products}} \tag{12}$$

As shown in Fig. 11a, the methane selectivity increases from 46% to 58% as the temperature increases from 227 to 400 °C and then drops slightly to 53% at 427 °C. Our simulation compares well with our experimental measured (Section 3.3) selectivity of methane as well as it increase with temperature in the range of 200–400 °C. However, our theoretical results indicate that there is an optimal temperature in the methane selectivity for CO hydrogenation over Rh/Mn/SiO_2 catalysts. Since most of experimental measurements were carried out in a very narrow temperature range including the present experimental work, the decrease in methane selectivity was not observed in the experiments. However, the simulated methane selectivity is qualitatively consistent with our experimental observation that the methane selectivity increases from ~37% at 256 °C to ~60% at 324 °C. Our simulations are also consistent with another previous observation, under similar operating conditions, that the selectivity to methane increases from 34.2% at 265 °C to 48.1% at 300 °C [62]. With increasing tempera-

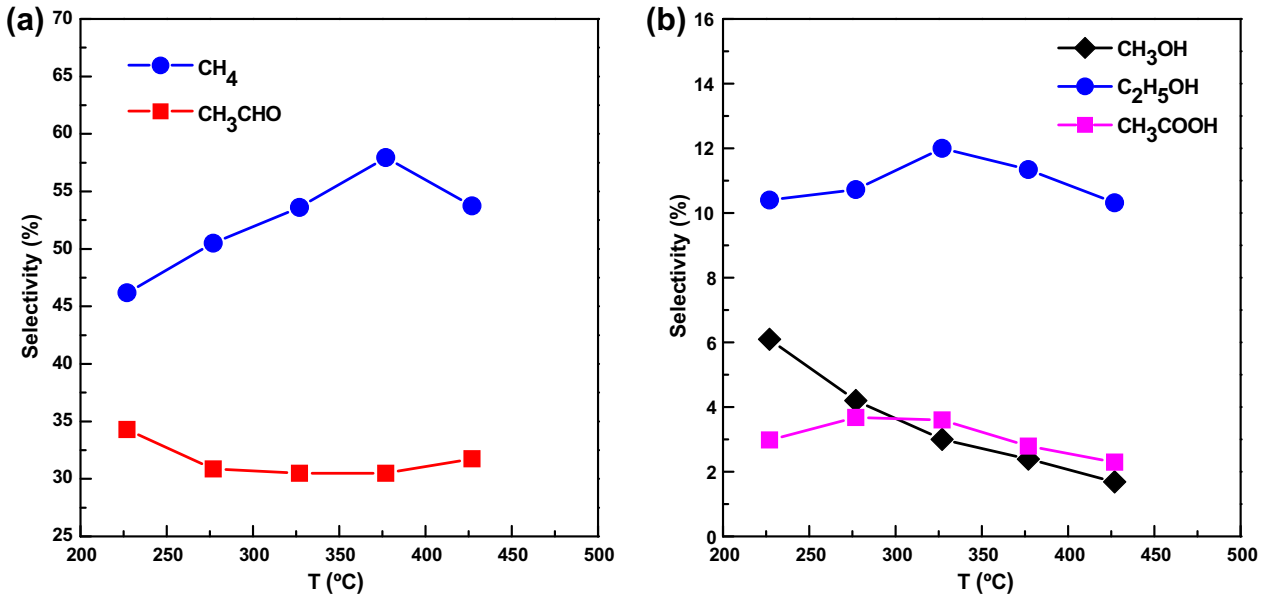

Fig. 11. The temperature dependence of selectivities of (a) methane and acetaldehyde; (b) methanol, ethanol, and acetic acid at $P = 2.0$ MPa ($P_{CO}/P_{H2} = 1{:}2$).

ture, the rates of methanation become faster than the rates of CO insertion steps. As such, the selectivity of CH_4 increases with the temperature. At higher temperature, the slight drops in CH_4 selectivity is due to the lower H coverage. Fig. 11b shows the selectivity for ethanol, methanol, and acetic acid. The selectivity to ethanol first increases from 10.4% to 12.0% until 227 °C, then decreases to 10.3% at 427 °C. This is also close to the results of 7.8% to 9.4% measured in this work. As seen in Table 1, the selectivity to ethanol slightly increases from 9.4% at 302 °C to 9.7% at 315 °C, then drops to 9.4% at 324 °C. On the other hand, the selectivity for methanol and acetic acid slightly decrease from 6.0% to 1.7% and 3.0% to 2.3% in the studied temperature range, respectively. If acetaldehyde and acetic acid are treated as the product C_2^+ oxygenates measured in the experiments, we found the simulated selectivity of C_2^+ oxygenates is about 33–38%, which also falls in our experimentally measured range of 19.4–43.2%. Our simulation results found that the increasing rates for CH_x hydrogenation steps are faster than the rate for the CO insertion step (CH + CO → CHCO) as the temperature is higher than 300 °C. To avoid the undesired methane product, CO hydrogenation over Rh-based catalysts for alcohols prefers to be operated at low temperature range (<300 °C) [8,11–14,20,38,62]. Our simulation results also show that the selectivity to ethanol increase with the temperature at the expenses of the selectivity to C_2^+ oxygenates and methanol. The total production for alcohols and other C_2^+ oxygenates decreases with the increasing temperature. This indicated that more C_2^+ hydrocarbons might be produced except for methane and ethane with the increasing temperature. This is reflected by the experimental observation that about 10–24% C_2^+ hydrocarbons generated in the reaction. Although we do not include the elementary steps leading to higher hydrocarbon species in the reaction network used in the simulations, we might expect that the increasing selectivities for C_2^+ hydrocarbons are at the expense of alcohols and other C_2^+ oxygenates at higher temperatures.

In addition to activity and selectivity, we found that the CO conversion increases with the temperature in accord with our experimental observations (see Table 1). CO conversion is defined as the ratio of the total consumed CO during the reaction against the initial CO concentration. As shown Fig. 12, the CO conversion dramatically increases from 0.98% to 13.4% as the temperature increases from 227 to 427 °C. This is consistent with our experiments that

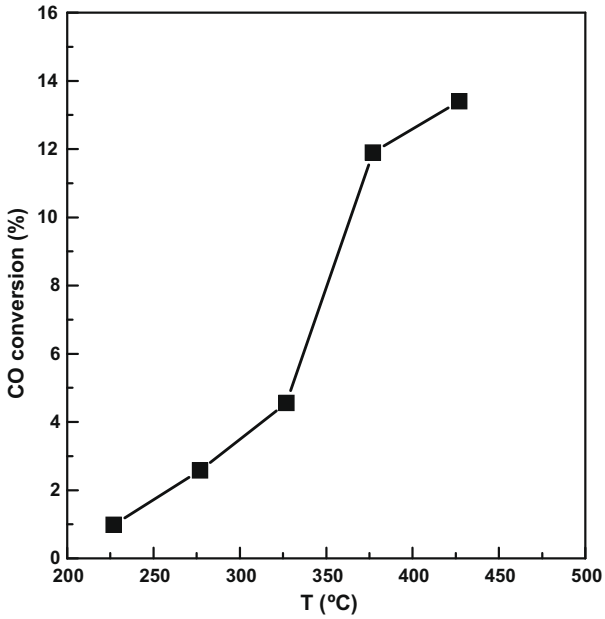

Fig. 12. The temperature dependence of CO conversion at $P = 2.0$ MPa ($P_{CO}/P_{H2} = 1{:}2$).

the rates for all the products increase with the increasing temperature.

The overall kinetics is not controlled merely by the intrinsic rate constants, but also by the surface coverage. The simulations allow us to explicitly track the identity and specific transformations for each surface species, as well as the average surface composition of different intermediates as functions of time and processing conditions. This information is subsequently used to establish the influence of specific intermediates on the kinetics. We find that CO and atomic H mostly cover the nanoparticle surface. The surface coverage of other reaction intermediates is very low (<0.05 ML). Herein, one monolayer (1 ML) is equivalent to one adsorbate per surface atom. The average surface coverages for atomic H and CO as a function of temperature are plotted in Fig. 13. The H coverage is 0.156 ML at 227 °C. As the temperature

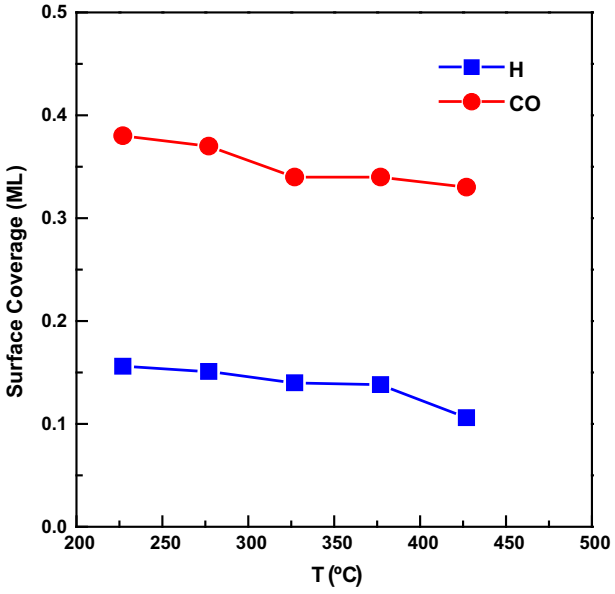

Fig. 13. The temperature dependence of averaged CO and atomic H coverages at $P = 2.0$ MPa ($P_{CO}/P_{H2} = 1{:}2$).

increases, the hydrogen atoms on the surface recombine to form H_2, which desorbs from the surface. At 427 °C, the hydrogen surface coverage decreases to 0.106 ML. The surface coverage of CO exhibits a similar trend. As the temperature increases from 227 to 427 °C, CO coverage decreases 0.381 to 0.334 ML. The availability of hydrogen and CO on the catalyst surface affects both the reaction rates and the selectivity of CO hydrogenation. We expect that effective adjustment of the surface coverage can dramatically influence the reaction progress and selectivities of products.

We also studied the effect of total reaction pressure on the CO hydrogenation kinetics over the $Rh/Mn/SiO_2$ catalyst nanoparticle. We found that the activity in term of TOFs is nearly the same under different total reaction pressures from 1.0 to 5.0 MPa, if the gas phase composition is the same ($P_{CO}/P_{H2} = 1{:}2$). However, the selectivity and conversion are changed with the total reaction pressure. For example, the CO conversion slightly decreases from 4.8% at 1.0 MPa to 4.1% at 5.0 MPa. It is important to note that in the present study we are mainly interested in a qualitative comparison between experiment and theory and that even though increasing the pressure will change the relative amounts of the product distributions it does not influence the essence of the chemistry occurring on the surface. As shown in Fig. 14, the methane selectivity decreases from 62.5% to 39.9%, while the ethanol selectivity significantly increases from 3.6% to 21.6% as the total pressure increases from 1.0 to 5.0 MPa at 300°C. We also find that the acetaldehyde selectivity increases from 25.3% to 32.5% as the total pressure increases. For methanol and acetic acid, the pressure effect is limited since the selectivity is relatively low, compared with other products. The pressure effect on the selectivity is also consistent with experimental observations [20]. This indicates that increasing the total reaction pressure will improve the selectivity of the desired product.

To further illustrate the Mn promoting effect on the ethanol production from CO hydrogenation over Rh-based catalysts, we compared the activities of CO hydrogenation on pure Rh and Rh/Mn (with 30% Mn composition) nanoparticles. The total pressure is 8 MPa with $P_{CO}/P_{H2} = 1{:}2$ in gas phase. The simulated temperature ranges from 290 to 330 °C. It is clearly shown in Fig. 15 that both TOFs of methane and ethanol increase with the addition of Mn. The calculated apparent activation energies are 43 and 36 kcal/mol for pure Rh and Rh/Mn nanoparticles. This indicates that the addition of Mn into Rh slightly increases the activity for ethanol production. Furthermore, we also found that the CO conversion increases from 30% on pure Rh to 60% on Rh/Mn alloy at 300 °C. This is in qualitative agreement with previous experimental observations [11]. As a result, our kinetic modeling captures the chemistry of CO hydrogenation to ethanol. The newly developed kinetic Monte Carlo simulation model is useful to predict the reaction kinetics for Rh-based catalysts with other promising promoters in the future.

5. Trends in the promotion effects on $Rh/M/SiO_2$ catalysts

Given the aforementioned modeling results that can qualitatively reproduce the reaction kinetics, we now try to gain more in-

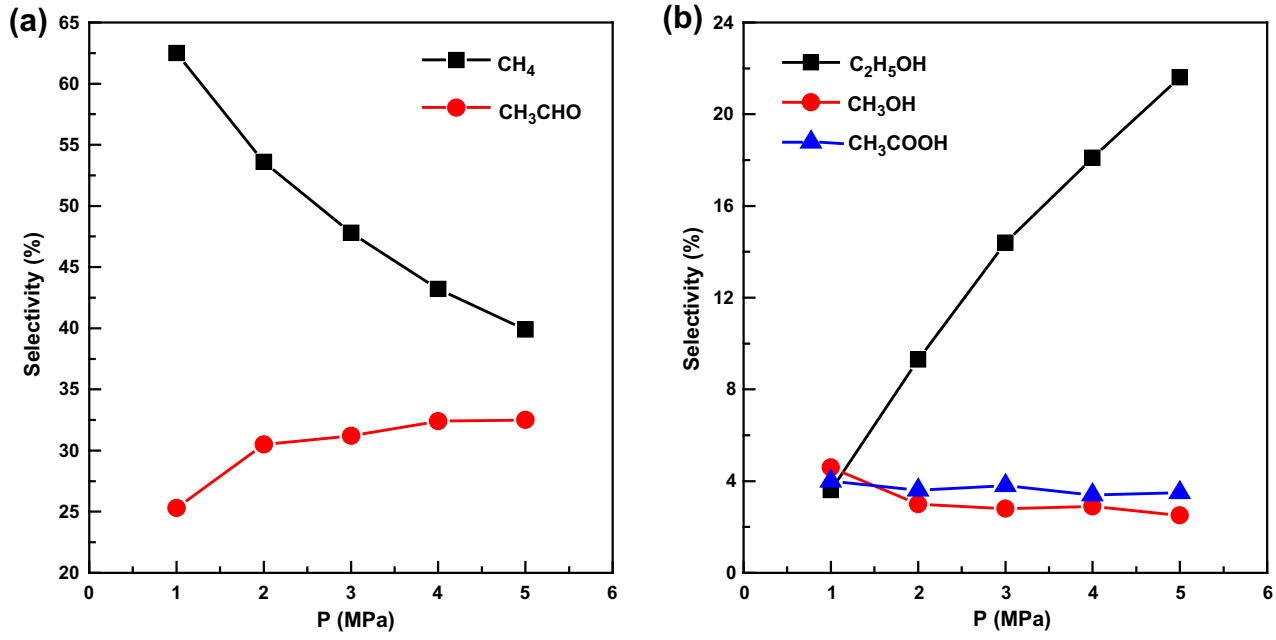

Fig. 14. The pressure dependence of selectivities at 300 °C ($P_{CO}/P_{H2} = 1{:}2$). (a) CH_4 and CH_3CHO; (b) C_2H_5OH, CH_3OH, and CH_3COOH.

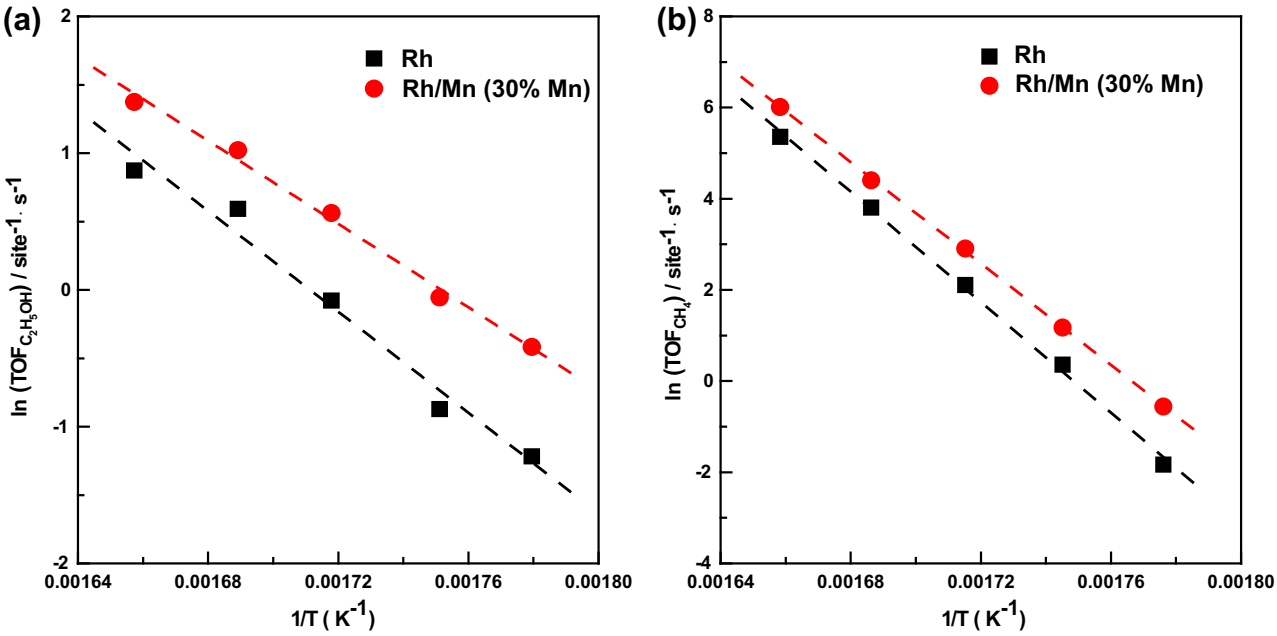

Fig. 15. The temperature dependence of TOFs at P = 8.0 MPa (P_{CO}/P_{H2} = 1:2). (a) Methane (b) ethanol.

sights into what this theoretical modeling can tell us about optimal catalyst design. For this, we consider that our model suggests that the role of the Mn promoters is to divert reactive flux from the methanation channel by providing an alternate low energy path, via inducing a lower barrier for CO insertion into CH (reaction R8), to form C_2^+ oxygenates at the early stage of hydrogenation of the adsorbed C. This aspect of the catalytic mechanism can be optimized by finding alternate promoters that can even further reduce CO insertion barriers.

We first digress to understand the underlying reason why the Mn promoter lowers the CO insertion barrier. At the outset of catalyst design, choices must be made from a vast array of possible elemental combinations using chemical intuition, theoretical predictions, and existing experimental observations. To this end, we sought to determine if there is some general correlation in choosing promoters with desired selectivity and productivity characteristics so that other promoters could be identified that will likely serve this same function. In this work, we hypothesize that the selectivity and productivity of the Rh/M/SiO_2 catalyst can be correlated to the electronegativity difference between Rh and the promoter M: given by $\Delta\chi = \chi_{Rh} - \chi_M$. This postulate is based on the observation that Mn embedded in a Rh matrix has a small partial positive charge, δ^+, making it a mildly Lewis acidic site which in turn favors low barriers for CO insertion reactions. To better understand this correlation, we performed DFT calculations to assess the influence of various promoters M (M = Ir, Ga, V, Mn, Ti, Sc, Ca, and Li) on the CO + CH → CHCO reaction. We assume that these promoters are being reduced to the metallic state within Rh dominant nanoparticles under the operating reaction conditions. We also note that some of promoters studied in this work might be difficult to reduce to the metallic state. This has been suggested by previous experimental results that are generally referring to the bulk oxide phases of those promoters. This is different from our model Rh/M nanoclusters where Rh is the dominant species in the nanoclusters. The surrounding Rh atoms could alleviate the difficulty of reduction for trace amounts of promoters (M) in the nanocluster. We believe it is possible that these promoters may be reduced and our idealized model of the Rh/M nanoparticle reflects this assumption. Fig. 16 shows the DFT calculated reaction barriers of CO + CH → CHCO on a (1 1 1) facet like surface over a 1.0 nm

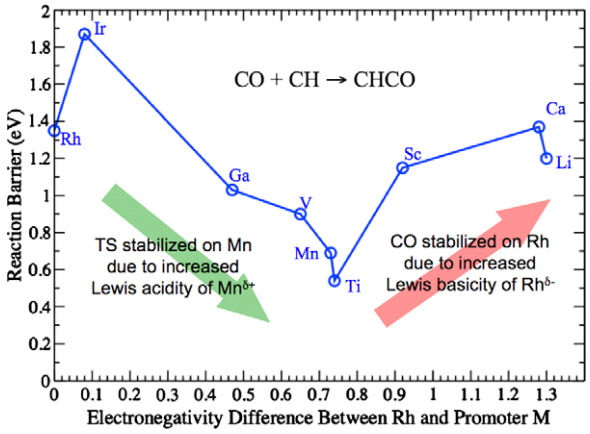

Fig. 16. DFT calculated activation barriers of CO + CH → CHCO on the Rh/M particles as a function of electronegativity differences ($\Delta\chi = \chi_{Rh} - \chi_M$, Pauling's scale) between Rh and various promoters M (M = Ir, Ga, V, Mn, Ti, Sc, Ca, and Li).

$Rh_{49}M_1$ catalyst nanoparticle as a function of electronegativity differences. It is found that the activation barrier for CO insertion into CH decreases with increasing $\Delta\chi$ up to 0.7, then increases as $\Delta\chi$ continues to increase. Alloying Ti with Rh with $\Delta\chi \sim 0.7$ (using Pauling's electronegativity scale), which has the lowest barrier for CO insertion, would be the best promoter candidate for increasing the selectivity and productivity of ethanol and other C_2^+ oxygenates by diverting reactive flux from the methane formation into the CO insertion pathways leading to the formation of C_2^+ oxygenates. As $\Delta\chi$ approaches 0.7, the transition state of CO insertion reaction is stabilized on the promoter site $M^{\delta+}$, which acts as Lewis acid site while the reactant CO becomes more stabilized on $Rh^{\delta-}$, which acts as Lewis base site and forms a stronger Rh–CO bond when $\Delta\chi$ exceeds 0.7.

In a recent review, Subramani and Gangwal [6] summarized the effects of various promoters M on the selectivity and productivity for ethanol production over Rh/M/SiO_2 catalysts. It is found that the promoters such as Mn, Ti, and V exhibit higher catalytic selectivity and productivity to ethanol production while the promoters

such as Zn, Cr, and Ga are not good for ethanol production. Clearly, our DFT calculations along with electronegativity differences show the same trend that was found through numerous experimental studies. Ti ($\Delta\chi = 0.7$) and V ($\Delta\chi = 0.65$) promoters yield the best selectivity and productivity. We also note that this general correlation also is consistent with our own experiments on ternary systems ($\Delta\chi = 0.6$–0.9) as well as the recent work of Goodwin et al. who found that the Rh–V–La combination on a silica support showed higher selectivity and activity to ethanol than to methanation [80]. Bearing this in mind, we suggest that the electronegativity difference between the base metal (Rh) and the promoter M may be used as kind of general criterion in choosing the optimum promoter candidate for ethanol synthesis from CO hydrogenation over the supported Rh/M catalysts.

6. Conclusions

In this work, we combined experimental measurements with first-principles-based kinetic modeling to investigate the reaction kinetics of ethanol synthesis from CO hydrogenation over silica supported Rh/Mn alloy catalysts. We proposed an alloy nanoparticle model wherein the promoter atom Mn exists in a binary alloy with Rh. This alloy model is supported by our XPS, TEM, and XRD characterization of the practical $Rh/Mn/SiO_2$ catalysts used in the experiments. On the basis of DFT calculated reaction energies of the Rh/MnO_x nanoparticles under *in situ* catalytic reducing conditions, a thermodynamic analysis of equilibrium constants suggest that the stability of the binary Rh/Mn alloy particle is preferred to a mixed $Rh–MnO_x$ system. We found that the alloying of Mn into Rh metal particle plays a critical role in the improvement of the activity and selectivity toward ethanol and other C_2^+ oxygenates. Our quantum chemical analysis of methane formation, along with three CO insertion steps forming $COCH_x$ species on the pure Rh and two Rh/Mn alloy nanoparticles indicates that methane formation is inevitable on the supported Rh/Mn catalysts because of low activation barriers for methanation. Doping Mn into Rh will not dramatically change the activation energy barriers to methane formation but will lower the barrier of CO insertion into CH although the activation barriers of CO insertion into CH_2 and CH_3 are still very high. Our KMC simulation results are in qualitative agreement with our experiments and previously reported data, indicating that the KMC simulation model developed in this work can capture the essential chemical and kinetic features of ethanol synthesis over the supported Rh/Mn catalysts. An optimum reaction temperature of 280 °C is found in the simulation where the highest ethanol selectivity (12%) is reached. Simulation results also show that methane production will decrease, as the reaction temperature is higher than 375 °C. With increasing the total reaction pressure, the ethanol selectivity increases while the methane selectivity decreases. This suggests that CO hydrogenation to ethanol on the $Rh/Mn/SiO_2$ catalyst is preferred under high-pressure condition. CO conversion also increases with the temperature but decreases with the total reaction pressure. The effects of various promoters (M) in Rh-based catalysts for ethanol synthesis from CO hydrogenation are further investigated using the proposed Rh/M alloy cluster model. We calculated the reaction barriers of CO + CH forming CHCO on Rh/M nanoparticles. The lower CO insertion barriers that correspond to the Rh/M catalysts with the electronegativity difference ($\Delta\chi \approx 0.7$) between Rh and the promoter have been found. Most importantly, this is coinciding with previous experimental observations that the promoters with $\Delta\chi \approx 0.7$ deliver the higher ethanol selectivity and productivity for the $Rh/M/SiO_2$ catalysts. We believe this general trend may set sort of criteria on improving current Rh-based catalysts for higher ethanol production.

Acknowledgments

This work was supported by the US Department of Energy Office of EERE Biomass Program under Contract DE-AC05-76RL01830, and was performed in part using EMSL, a national scientific user facility sponsored by the Department of Energy's Office of Biological and Environmental Research located at Pacific Northwest National Laboratory (PNNL). PNNL is operated for the US DOE by Battelle Memorial Institute under Contract No. DE-AC06-76RLO-1830. Computational resources were provided by the Molecular Science Computing Facility (EMSL) and the National Energy Research Scientific Computing Center (NERSC) at Lawrence Berkeley National Laboratory.

Appendix A. Supplementary material

Supplementary data associated with this article can be found, in the online version, at doi:10.1016/j.jcat.2010.02.020.

References

[1] J.R. Rostrup-Nielsen, Science 308 (2005) 1421.
[2] L.D. Schmidt, P.J. Dauenhauer, Nature 447 (2007) 914.
[3] C.S. Song, Catal. Today 115 (2006) 2.
[4] A. Ahmed, R.S. Lewis, Biotechnol. Bioeng. 97 (2007) 1080.
[5] J.J. Spivey, A. Egbebi, Chem. Soc. Rev. 36 (2007) 1514.
[6] V. Subramani, S.K. Gangwal, Energy Fuels 22 (2008) 814.
[7] M.M. Bhasin, Catal. Lett. 59 (1999) 1.
[8] M.M. Bhasin, W.J. Bartley, P.C. Ellgen, T.P. Wilson, J. Catal. 54 (1978) 120.
[9] R. Burch, M.I. Petch, Appl. Catal. A – Gen. 88 (1992) 39.
[10] R. Burch, M.I. Petch, Appl. Catal. A – Gen. 88 (1992) 77.
[11] Progress in C1 Chemistry in Japan, Elsevier Science Ltd., Amsterdam, 1989.
[12] M.A. Gerber, J.F. White, D.J. Stevens, Mixed Alcohol Synthesis Catalyst Screening, Pacific Northwest National Laboratory, Richland, Washington, 2007.
[13] P.C. Ellgen, W.J. Bartley, M.M. Bhasin, T.P. Wilson, Adv. Chem. Ser. 178 (1979) 147.
[14] T.P. Wilson, P.H. Kasai, P.C. Ellgen, J. Catal. 69 (1981) 193.
[15] F.G.A. Vandenberg, J.H.E. Glezer, W.M.H. Sachtler, J. Catal. 93 (1985) 340.
[16] H.Y. Luo, P.Z. Lin, S.B. Xie, H.W. Zhou, C.H. Xu, S.Y. Huang, L.W. Lin, D.B. Liang, P.L. Yin, Q. Xin, J. Mol. Catal. A – Chem. 122 (1997) 115.
[17] M. Bowker, Catal. Today 15 (1992) 77.
[18] S.S.C. Chuang, R.W. Stevens, R. Khatri, Top. Catal. 32 (2005) 225.
[19] W.M.H. Sachtler, M. Ichikawa, J. Phys. Chem. 90 (1986) 4752.
[20] Y. Wang, H.Y. Luo, D.B. Liang, X.H. Bao, J. Catal. 196 (2000) 46.
[21] Y. Choi, P. Liu, J. Am. Chem. Soc. 131 (2009) 13054.
[22] P.R. Watson, G.A. Somorjai, J. Catal. 72 (1981) 347.
[23] S.S.C. Chuang, S.I. Pien, J. Catal. 138 (1992) 536.
[24] S.S.C. Chuang, S.I. Pien, J. Catal. 135 (1992) 618.
[25] E. Shustorovich, H. Sellers, Surf. Sci. Rep. 31 (1998) 5.
[26] J. Gao, X.H. Mo, A.C.Y. Chien, W. Torres, J.G. Goodwin, J. Catal. 262 (2009) 119.
[27] M.A. Haider, M.R. Gogate, R.J. Davis, J. Catal. 261 (2009) 9.
[28] X.H. Mo, J. Gao, J.G. Goodwin, Catal. Today 147 (2009) 139.
[29] X.H. Mo, J. Gao, N. Umnajkaseam, J.G. Goodwin, J. Catal. 267 (2009) 167.
[30] J.P. Perdew, K. Burke, M. Ernzerhof, Phys. Rev. Lett. 77 (1996) 3865.
[31] V.I. Anisimov, J. Zaanen, O.K. Andersen, Phys. Rev. B 44 (1991) 943.
[32] G. Lippert, J. Hutter, M. Parrinello, Mol. Phys. 92 (1997) 477.
[33] J. VandeVondele, M. Krack, F. Mohamed, M. Parrinello, T. Chassaing, J. Hutter, Comput. Phys. Commun. 167 (2005) 103.
[34] G. Henkelman, B.P. Uberuaga, H. Jonsson, J. Chem. Phys. 113 (2000) 9901.
[35] G. Mills, H. Jonsson, G.K. Schenter, Surf. Sci. 324 (1995) 305.
[36] J.W. Niemantsverdriet, Spectroscopy in Catalysis, Wiley-VCH, Weinheim, 2007.
[37] D.A. McQaurrie, Statistical Mechanics, University Science Books, New York, 2000.
[38] M. Ojeda, M.L. Granados, S. Rojas, P. Terreros, F.J. Garcia-Garcia, J.L.G. Fierro, Appl. Catal. A – Gen. 261 (2004) 47.
[39] Y. Wang, Z. Song, D. Ma, H.Y. Luo, D.B. Liang, X.H. Bao, J. Mol. Catal. A – Chem. 149 (1999) 51.
[40] Z.P. Liu, P. Hu, M.H. Lee, J. Chem. Phys. 119 (2003) 6282.
[41] V.K. Medvedev, V.S. Kulik, V.I. Chernyi, Y. Suchorski, Vacuum 48 (1997) 341.
[42] Z.P. Liu, P. Hu, J. Chem. Phys. 114 (2001) 8244.
[43] Z.P. Liu, P. Hu, J. Am. Chem. Soc. 123 (2001) 12596.
[44] F. Abild-Pedersen, J. Greeley, F. Studt, J. Rossmeisl, T.R. Munter, P.G. Moses, E. Skulason, T. Bligaard, J.K. Norskov, Phys. Rev. Lett. 99 (2007).
[45] B.S. Bunnik, G.J. Kramer, J. Catal. 242 (2006) 309.
[46] J. Chen, Z.P. Liu, J. Am. Chem. Soc. 130 (2008) 7929.
[47] O.R. Inderwildi, S.J. Jenkins, D.A. King, J. Am. Chem. Soc. 129 (2007) 1751.
[48] A. Kokalj, N. Bonini, C. Sbraccia, S. de Gironcoli, S. Baroni, J. Am. Chem. Soc. 126 (2004) 16732.

[49] N. Kruse, G.K. Chuah, G. Abend, D.L. Cocke, J.H. Block, Surf. Sci. 189 (1987) 832.
[50] T. Bligaard, J.K. Norskov, S. Dahl, J. Matthiesen, C.H. Christensen, J. Sehested, J. Catal. 224 (2004) 206.
[51] M. Boudart, The Kinetics of Chemical Processes, Butterworth–Heinemann, Boston, 1991.
[52] P. Ferrin, D. Simonetti, S. Kandoi, E. Kunkes, J.A. Dumesic, J.K. Norskov, M. Mavrikakis, J. Am. Chem. Soc. 131 (2009) 5809.
[53] G. Fratesi, P. Gava, S. de Gironcoli, J. Phys. Chem. C 111 (2007) 17015.
[54] A. Kokalj, N. Bonini, S. de Gironcoli, C. Sbraccia, G. Fratesi, S. Baroni, J. Am. Chem. Soc. 128 (2006) 12448.
[55] Z.P. Liu, P. Hu, J. Am. Chem. Soc. 125 (2003) 1958.
[56] X.F. Ma, H.Q. Deng, M.M. Yang, W.X. Li, J. Chem. Phys. 129 (2008) 244711.
[57] A. Resta, J. Gustafson, R. Westerstrom, A. Mikkelsen, E. Lundgren, J.N. Andersen, M.M. Yang, X.F. Ma, X.H. Bao, W.X. Li, Surf. Sci. 602 (2008) 3057.
[58] E. Vesselli, A. Baraldi, G. Comelli, S. Lizzit, R. Rosei, ChemPhysChem 5 (2004) 1133.
[59] M.M. Yang, X.H. Bao, W.X. Li, J. Chem. Phys. 127 (2007) 024705.
[60] M.M. Yang, X.H. Bao, W.X. Li, J. Phys. Chem. C 111 (2007) 7403.
[61] M.M. Yang, X.H. Bao, W.X. Li, Chin. J. Catal. 29 (2008) 75.
[62] J.L. Hu, Y. Wang, C.S. Cao, D.C. Elliott, D.J. Stevens, J.F. White, Catal. Today 120 (2007) 90.
[63] P.Z. Lin, D.B. Liang, H.Y. Luo, C.H. Xu, H.W. Zhou, S.Y. Huang, L.W. Lin, Appl. Catal. A – Gen. 131 (1995) 207.
[64] A.K. Datye, J. Catal. 216 (2003) 144.
[65] A. Christensen, A.V. Ruban, P. Stoltze, K.W. Jacobsen, H.L. Skriver, J.K. Norskov, F. Besenbacher, Phys. Rev. B 56 (1997) 5822.
[66] E. Christoffersen, P. Stoltze, J.K. Norskov, Surf. Sci. 505 (2002) 200.
[67] A.V. Ruban, H.L. Skriver, J.K. Norskov, Phys. Rev. B 59 (1999) 15990.
[68] L.D. Kieken, M. Neurock, D.H. Mei, J. Phys. Chem. B 109 (2005) 2234.
[69] D. Mei, P.A. Sheth, M. Neurock, C.M. Smith, J. Catal. 242 (2006) 1.
[70] D.H. Mei, Q.F. Ge, M. Neurock, L. Kieken, J. Lerou, Mol. Phys. 102 (2004) 361.
[71] D.H. Mei, E.W. Hansen, M. Neurock, J. Phys. Chem. B 107 (2003) 798.
[72] M. Mavrikakis, M. Baumer, H.J. Freund, J.K. Norskov, Catal. Lett. 81 (2002) 153.
[73] F.B. de Mongeot, A. Toma, A. Molle, S. Lizzit, L. Petaccia, A. Baraldi, Phys. Rev. Lett. 97 (2006).
[74] E. Hansen, M. Neurock, Surf. Sci. 441 (1999) 410.
[75] E. Hansen, M. Neurock, J. Phys. Chem. B 105 (2001) 9218.
[76] E.W. Hansen, M. Neurock, J. Catal. 196 (2000) 241.
[77] E.W. Hansen, M. Neurock, Surf. Sci. 464 (2000) 91.
[78] M. Beutl, J. Lesnik, K.D. Rendulic, Surf. Sci. 429 (1999) 71.
[79] E. Vesselli, A. Baraldi, F. Bondino, G. Comelli, M. Peressi, R. Rosei, Phys. Rev. B 70 (2004) 115404.
[80] J. Gao, X. Mo, A.C.-Y. Chien, W. Torres, J.G. Goodwin Jr., J. Catal. 262 (2009) 119.